Czech Technical University in Prague
Faculty of Nuclear Sciences and Physical Engineering

**Department of Physics**
**Study programme: Nuclear and Particle Physics**

# Longitudinal profiles of the highest energy cosmic-ray air showers measured at the Pierre Auger Observatory

DIPLOMA THESIS

Author: Bc. Nikolas Denner
Supervisor: Ing. Jakub Vícha, Ph.D.
Academic year: 2022

České vysoké učení technické v Praze
Fakulta jaderná a fyzikálně inženýrská

**Katedra fyziky**
**Studijní program: Jaderná a částicová fyzika**

# Podélné profily atmosférických spršek kosmického záření nejvyšších energií pozorované na Observatoři Pierra Augera

DIPLOMOVÁ PRÁCE

Vypracoval: Bc. Nikolas Denner
Vedoucí práce: Ing. Jakub Vícha, Ph.D.
Rok: 2022

ČESKÉ VYSOKÉ UČENÍ TECHNICKÉ V PRAZE
**FAKULTA JADERNÁ A FYZIKÁLNĚ INŽENÝRSKÁ**
PRAHA 1 - STARÉ MĚSTO, BŘEHOVÁ 7 - PSČ 115 19

*Katedra:* fyziky *Akademický rok:* 2021/2022

# ZADÁNÍ DIPLOMOVÉ PRÁCE

*Student:* Bc. Nikolas Denner

*Studijní program:* Jaderná a částicová fyzika

*Název práce: (česky)* Podélné profily atmosférických sprškek kosmického záření nejvyšších energií pozorované na Observatoři Pierra Augera

*Název práce: (anglicky)* Longitudinal profiles of the highest energy cosmic-ray air showers measured at the Pierre Auger Observatory

*Pokyny pro vypracování:*

1) Rekonstrukční algoritmy sprškek kosmického záření na Observatoři Pierra Augera.
2) Analýza podélných profilů sprškek standardní hybridní rekonstrukcí.
3) Analýza podélných profilů sprškek hybridních událostí s osou získanou z povrchového detektoru.
4) Analýza podélných profilů sprškek stereo rekonstrukcí.
5) Kombinace výsledků.

*Doporučená literatura:*

[1] A. Aab, et al.: The Pierre Auger cosmic ray observatory, NIM A 798 (2015) 172-213

[2] S. Argiro, et al.: The Offline software framework of the Pierre Auger Observatory, NIM A 580 (2007) 1485-1496

[3] A. Aab, et al.: Depth of maximum of air-shower profiles at the Pierre Auger Observatory: Measurements at energies above 10^17.8 eV, Phys. Rev. D 90 (2014) 122005

[4] A. Aab, et al.: Spectral calibration of the fluorescence telescopes of the Pierre Auger Observatory, Astropart. Phys. 95 (2017) 44-56

*Jméno a pracoviště vedoucího diplomové práce:*

Ing. Jakub Vícha, Ph.D., Fyzikální ústav AV ČR, v. v. i.

Jméno a pracoviště konzultanta diplomové práce:
RNDr. Vladimír Novotný, Ph.D., Fyzikální ústav AV ČR, v. v. i.

*Datum zadání diplomové práce:* 20.10.2021

*Termín odevzdání diplomové práce:* 02.05.2022

*Doba platnosti zadání je dva roky od data zadání.*

.....
*garant studijního programu*

.....
*vedoucí katedry*

ČESKÉ VYSOKÉ UČENÍ TECHNICKÉ V PRAZE
Fakulta jaderná a fyzikálně inženýrská

.....
*děkan*

*V Praze dne* 20.10.2021

**Prohlášení**

Prohlašuji, že jsem svou diplomovou práci vypracoval samostatně a použil jsem pouze podklady (literaturu, projekty, SW atd.) uvedené v přiloženém seznamu.

Nemám závažný důvod proti použití tohoto školního díla ve smyslu § 60 Zákona č. 121/2000 Sb., o právu autorském, o právech souvisejících s právem autorským a o změně některých zákonů (autorský zákon).

V Praze dne .....  .....

Bc. Nikolas Denner

**Acknowledgements**

I would like to thank my supervisor Ing. Jakub Vícha, Ph.D for his insight into the researched topic and his educational comments. I would also like to thank RNDr. Vladimír Novotný, Ph.D. for his help with the problems connected with the Auger Offline framework, Dr. Alexey Yushkov for the access to the CORSIKA simulated showers, and mostly to my girlfriend, Karolína Syrokvaš, for her unconditional and endless mental support.

Bc. Nikolas Denner

*Název práce:*

**Podélné profily atmosférických sprškek kosmického záření nejvyšších energií pozorované na Observatoři Pierra Augera**

*Autor:* Bc. Nikolas Denner

*Studijní program:* Jaderná a částicová fyzika
*Druh práce:* Diplomová práce

*Vedoucí práce:* Ing. Jakub Vícha, Ph.D.
Oddělení astročásticové fyziky, Fyzikální ústav Akademie věd České republiky, v. v. i.
*Konzultant:* RNDr. Vladimír Novotný, Ph.D.
Ústav částicové a jaderné fyziky, Matematicko-fyzikální fakulta, Univerzita Karlova

*Abstrakt:* Alternativní přístupy k rekonstrukci dat nasbíraných pomocí fluorescenčních teleskopů na Observatoři Pierra Augera mají potenciál rozšířit počet detekovaných sprškek kosmického záření. Toto rozšíření má obzvlášť velký význam pro ultra-vysoko-energetické sprškky, které mají kvůli prudce se snižujícímu toku částic s jejich zvyšující se energií malou statistiku. Zvýšení počtu těchto dat v analýze vlastností kosmického záření by mohlo vést k jejich lepšímu porozumění. Tato práce se zabývá srovnáním dvou alternativních rekonstrukčních metod a jedné standardně aplikované. Jejich společným použitím lze navýšit počet událostí s energií nad $10^{19.2}$ eV o více než 10%.

*Klíčová slova:* Kosmické záření, atmosférické sprškky částic, Observatoř Pierra Augera, podélný profil, hybridní rekonstrukce, stereo rekonstrukce, hloubka maxima sprškky.

*Title:*

**Longitudinal profiles of the highest energy cosmic-ray air showers measured at the Pierre Auger Observatory**

*Author:* Bc. Nikolas Denner

*Abstract:* Alternative reconstruction methods of the Pierre Auger Observatory data measured by its fluorescence telescopes have the potential to extend the number of detected cosmic-ray showers. This extension is of great importance especially for ultra-high-energy showers burdened by very low statistic due to the steeply decreasing flux of particles with their increasing energy. The increase of the data set used for the analysis of cosmic-ray properties could lead to a better understanding of the physics behind this phenomenon. This work focuses on a comparison of two alternative reconstruction methods with one standard method. By applying the alternative reconstruction methods, the data set of events above energies of $10^{19.2}$ eV can be increased by more than 10%.

*Key words:* Cosmic rays, air showers, Pierre Auger Observatory, longitudinal profile, hybrid reconstruction, stereo reconstruction, depth of shower maximum.

# Contents

# Introduction

Cosmic rays are high-energy particles originating outside the Earth. Throughout the last century, the study of cosmic rays has significantly contributed to the development of particle physics. These contributions and also the discovery of the cosmic rays itself are briefly described in the first section of the first chapter. The next two sections introduce the properties of cosmic rays and the extensive air showers developing upon interactions of cosmic rays with the Earth's atmosphere; the detection of these extensive air showers together with a few examples of different types of cosmic-ray experiments is described in the last section of the first chapter.

The energies of the cosmic rays can reach up to $10^{20}$ eV. At these ultra-high energies, the flux of the particles is about 1 particle per km$^2$ per century. To be able to detect the particles from the end of the cosmic-ray energy spectrum, one needs to employ detectors spread out over huge areas. One such experiment is the Pierre Auger Observatory which uses a surface detector (SD) array as well as a fluorescence detector (FD) for cosmic-ray shower detection. A sufficient description of the data acquisition at the Pierre Auger Observatory as well as the Auger Offline framework used for data reconstruction is given in the second chapter.

A very important part of the cosmic-ray shower studies is played by simulations of these air cascades. Extensive air-shower simulations are done via codes based on the Monte Carlo method simulating the development of the shower throughout the atmosphere. For description of interactions between the shower particles and the atmosphere, the simulation codes need to employ external hadronic interaction models. These models are developed to correctly describe the available data from particle accelerators and to extrapolate the behaviour of the interactions to energies observed only in cosmic-ray showers. Three of the highest-energy hadronic interaction models are QGSJET-II, SIBYLL and EPOS and they are briefly introduced in the third chapter together with the CORSIKA simulation code used for the following analysis.

The main focus of this work is on the comparison and analysis of a potential combination of three different reconstruction methods of the Pierre Auger Observatory data that incorporate the FD signal. These methods are used for the reconstruction of either hybrid data, which are showers seen by both the SD and the FD, and stereo data, which are showers seen by at least 2 out of 4 FD sites. From the FD signal we are able to reconstruct the longitudinal profile of the shower giving us the calorimetric energy of the shower as well as the depth at which the shower deposits maximum of its energy. This so-called depth of the shower maximum is referred to as $X_{\mathrm{max}}$. The fourth chapter is dedicated to the description of the longitudinal profile of the shower and its properties as well as to a more detailed introduction of

the three reconstruction methods.

In the fifth chapter we analyse the differences between the three methods in the reconstruction of the depth of the shower maximum $X_{\mathrm{max}}$ and the calorimetric energy $E_{\mathrm{cal}}$. We do this by applying the methods on CORSIKA simulated showers and comparing the properties reconstructed by one of the alternative methods with the standardly used hybrid reconstruction method. We also show the biases between the reconstructed and Monte Carlo simulated properties and their resolutions and propose simple correction factors for the $X_{\mathrm{max}}$ reconstructed by the alternative methods with respect to the HD reconstructed $X_{\mathrm{max}}$. In the last chapter we apply the proposed correction factors on real Observatory data and discuss the number of new events that can be added to the overall analysis of cosmic-ray showers by using the two alternative reconstruction methods.

# Chapter 1

# Cosmic rays

## 1.1 History

The first hint about the existence of the cosmic rays appeared at the end of the 18th century [1], when C. A. Coulomb noticed that insulated electroscopes are able to discharge spontaneously. Coulomb attributed this effect to the contact of the electroscopes with air. About a hundred years later, around the time when spontaneous radioactivity was discovered by Becquerel, scientists started speculating that this phenomenon may be caused by ionizing radiation. Among the assumptions about possible terrestrial origin of such ionization, Scottish physicist C. T. R. Wilson, who later invented the cloud chamber, suggested that its origin could as well be extraterrestrial. Wilson investigated the electroscope discharge above and under the ground and compared the results [2]. However, he did not observe any significant result, as the difference between both values was within the range of the experimental uncertainties. This led to the extraterrestrial explanation of the ionization being discarded for almost a decade.

One of the most favored explanations of the ionizing radiation was radioactivity from the Earth's crust. This assumption was inspected by a few physicists, who tried to measure the decrease of the ionization rate with increasing altitude. One of those was German scientist T. Wulf, who measured the ionization rate on the top of the Eiffel tower[1]. However, his results did not match the expected decrease in the ionization rate. Physicists who wanted to shine more light on this mysterious ionization therefore had to measure the ionization rate at much higher altitudes.

An informative result was finally achieved by Austrian physicist V. F. Hess, who measured the dependence of the ionization rate on the altitude during several balloon flights up to 5 km in the years 1911 and 1912. He found out that the rate increased with the altitude [4, 5], implying its extraterrestrial origin. He also deduced that the source of the ionizing radiation is not mainly the Sun, as the rate during the night did not differ from the rate during the day. After that, a German physicist W. Kolhörster carried out flights up to more than 9 km and confirmed Hess' results.

For more than 10 years after the Hess' observation, it was thought that the ionizing

[1]The highest point a person can go up to on the Eiffel tower is close to 300 m [3].

radiation, which came to be called "cosmic rays", consisted of $\gamma$ radiation. An experiment conducted between years 1927 and 1928 by Dutch physicist J. Clay showed that the rate of ionization changed with latitude [6]. This result made it obvious that the radiation was electrically charged. An even more illuminating result was achieved in 1933 by three independent experiments [7, 8]. These experiments found out that the rate of cosmic rays near the Equator was higher in direction from the West resulting in what we call today the East-West effect. Such observations made it clear that the charge of the incoming cosmic rays was mostly positive.

The next crucial discovery uncovering the mystery of cosmic rays was conducted first in 1934 by Italian physicist B. Rossi, who recorded pulses at almost identical times on two distant Geiger-Müller counters. He deduced that it was caused by an extensive particle shower. However, Rossi did not study this phenomenon further. The same observation was made four years later by French physicist P. Auger. Auger, unfamiliar with the results of Rossi, detected coincidences on two counters with increasing distances up to 300 m [9]. He attributed this effect to air showers initiated by primary cosmic-ray particles and estimated the energy of these primary particles to be about $10^{15}$ eV.

In the following years, the study of cosmic rays pioneered the modern particle physics with the observations of many new particles originated in air showers. Physicists working in this field were searching mainly for the so-called Yukawa particle that could confirm the theory of strong interactions [10] proposed by young Japanese physicist H. Yukawa. During this search, a particle with mass in accordance with the theory was found [11]. This particle decayed with a lifetime higher by two orders of the magnitude in comparison with the theoretical Yukawa particle. Another discrepancy was the high penetrating power of this particle. Later, it was confirmed that this particle was not the proposed mediator of the strong interaction, but it was the "heavier brother" of the electron, nowadays known as muon. The actual Yukawa particle, called pion (or $\pi$ meson), was detected in 1947 [12] with the use of cosmic rays. This detection confirmed the existence of both positive and negative pions. It was also observed that pions decay into muons with a subsequent decay into electrons with some missing energy carried away by neutrinos.

In the 1950s, particle accelerators became the main source of particle physics studies. After the Cosmic Ray Conference in 1953, many cosmic-ray physicists transferred to the accelerator field, but that did not mean the end for the cosmic-ray physics. Throughout the second half of the $20^{\text{th}}$ century, many new cosmic-ray experiments arose and the study of the cosmic-rays is still relevant to this day.

One of the most recent discoveries regarding the cosmic rays was achieved by the Pierre Auger Collaboration in 2017 [13]. From the distribution of the directions of the primary cosmic rays with energies above 8 EeV, detected through the air showers, the Collaboration discovered a dipole-like anisotropy with direction of the dipole far away ($\approx$120°) from the direction to the center of our Galaxy. The dipole can be seen in Figure 1.1. This result signified that the highest-energy cosmic rays do not originate in our Galaxy.

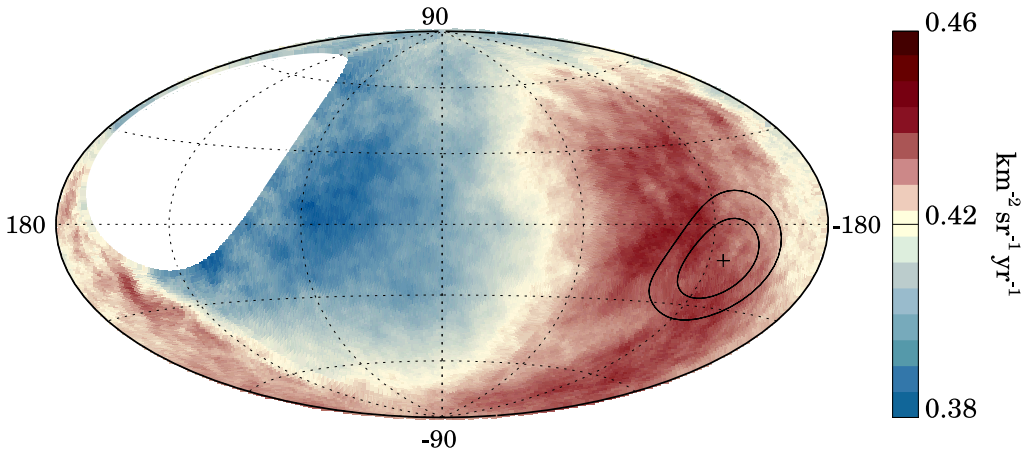


Figure 1.1: Flux of particles with energies above 8 EeV measured by the Pierre Auger Observatory. The flux is given in Galactic coordinates having the Galactic center at the origin. The cross corresponds to the dipole direction with 68% and 95% confidence-level regions given by the contours. From [13], modified.

## 1.2 Properties

The cosmic-ray particles strike the Earth's atmosphere continuously. The collisions of these particles with atmospheric nuclei initiate air showers, analogical to the particle cascades produced in calorimeters. By detecting and reconstructing such air showers, some of the properties of the original cosmic-ray particles can be obtained. The main properties include its mass, energy and the direction from which it hit the Earth's atmosphere. The particle that initiates the shower is referred to as the primary particle, whereas all of the particles that constitute the shower are called secondary particles.

The energy spectrum of cosmic rays (see Figure 1.2) goes up to values above $10^{20}$ eV. It can be divided into several regions separated by the change of slope of the flux. The first change occurs in a so-called knee (about $3{\cdot}10^{15}$ eV [14]). Statistically, we should record approximately one cosmic-ray particle with such energy on an area of 1 m$^2$ in a year. Another change of the slope occurs in a second knee (about $4{\cdot}10^{17}$ eV [15]), followed by an ankle (about $5 \cdot 10^{18}$ eV [16]). In this case, one cosmic-ray particle with such energy should statistically be observed on an area of 1 km$^2$ in about one year. After the slight increase of the flux at the ankle, the spectrum steepens again in a second ankle (about $1.3 \cdot 10^{19}$ eV [16]) and at energies above $5 \cdot 10^{19}$ eV [16], the flux is finally suppressed. The rate of cosmic-ray particles with energies from the end of the spectrum is one particle per 1 km$^2$ per century. One of the causes of the suppression of the cosmic-ray flux at energies around $5 \cdot 10^{19}$ eV is an effect called the GZK cutoff[2].

The dependence of the cosmic-ray flux $J$ on its energy $E$ can be described by a

[2]In 1966, Greisen [17] and Zatsepin and Kuzmin [18] calculated an upper bound for energy of cosmic rays coming from distant sources. This upper bound is due to interaction of cosmic rays with the cosmic microwave background.

power law [19]

$$J(E) \propto E^{-\gamma}, \tag{1.1}$$

where $\gamma$ is called a spectral index and changes throughout the energy range in the following way:

- For $E < 3 \cdot 10^{15}$ eV, the spectral index is $\gamma \approx 2.7$.
- For $3 \cdot 10^{15}$ eV $< E < 4 \cdot 10^{17}$ eV, the spectral index is $\gamma \approx 3.1$.
- For $4 \cdot 10^{17}$ eV $< E < 5 \cdot 10^{18}$ eV, the spectral index is $\gamma \approx 3.29$.
- For $5 \cdot 10^{18}$ eV $< E < 1.3 \cdot 10^{19}$ eV, the spectral index is $\gamma \approx 2.51$.
- For $1.3 \cdot 10^{19}$ eV $< \ E \ < \ 4.6 \cdot 10^{19}$ eV, the spectral index is $\gamma \approx 3.05$.
- For $5 \cdot 10^{19}$ eV $< E$, the spectral index is $\gamma \approx 5.1$.

Parts of the energy spectrum with different values of the spectral index are dominated by different cosmic-ray sources, acceleration mechanisms or effects of cosmic-ray propagation. The lowest-energy primaries are mostly coming from the Sun, primaries with energies between the knee and the second knee are mostly radiated by astrophysical objects in our Galaxy (considerable part is attributed to supernovae), and primaries with energies above the ankle are extragalactic. Cosmic rays with energies above $10^{18}$ eV are referred to as ultra-high-energy cosmic rays (UHECR) and even to this day, sources of such particles are unknown.

Concerning the cosmic-ray acceleration, there are several types of mechanisms that can provide energy to the particles. Charged particles may be accelerated in electric fields induced by time-variable magnetic fields. Another possibility is the so-called second-order Fermi acceleration [21]. The main idea of this mechanism is scattering and isotropization of a cosmic ray in a magnetic cloud with velocity $\beta$. Such cloud could be e.g. a shock wave produced by collapse of a star. The mean relative change of energy of the cosmic ray in such cloud is [3]

$$\left\langle \frac{\Delta E}{E} \right\rangle \approx \frac{4}{3} \cdot \beta^2. \tag{1.2}$$

Similar mechanism is a diffusive shock acceleration (or the first-order Fermi mechanism). In this case, the final direction of the cosmic-ray particle is not isotropic and the final relative change of energy is

$$\frac{\Delta E}{E} \approx \frac{4}{3} \cdot \beta. \tag{1.3}$$

The propagation of cosmic rays is mostly affected by their interactions with magnetic fields. While trajectories of photons and neutrinos are not altered by electromagnetic force at all, the trajectories of hadrons and charged leptons can be isotropized. Low-energy cosmic rays can be affected even by the magnetic field of the Earth resulting in the East-West effect.

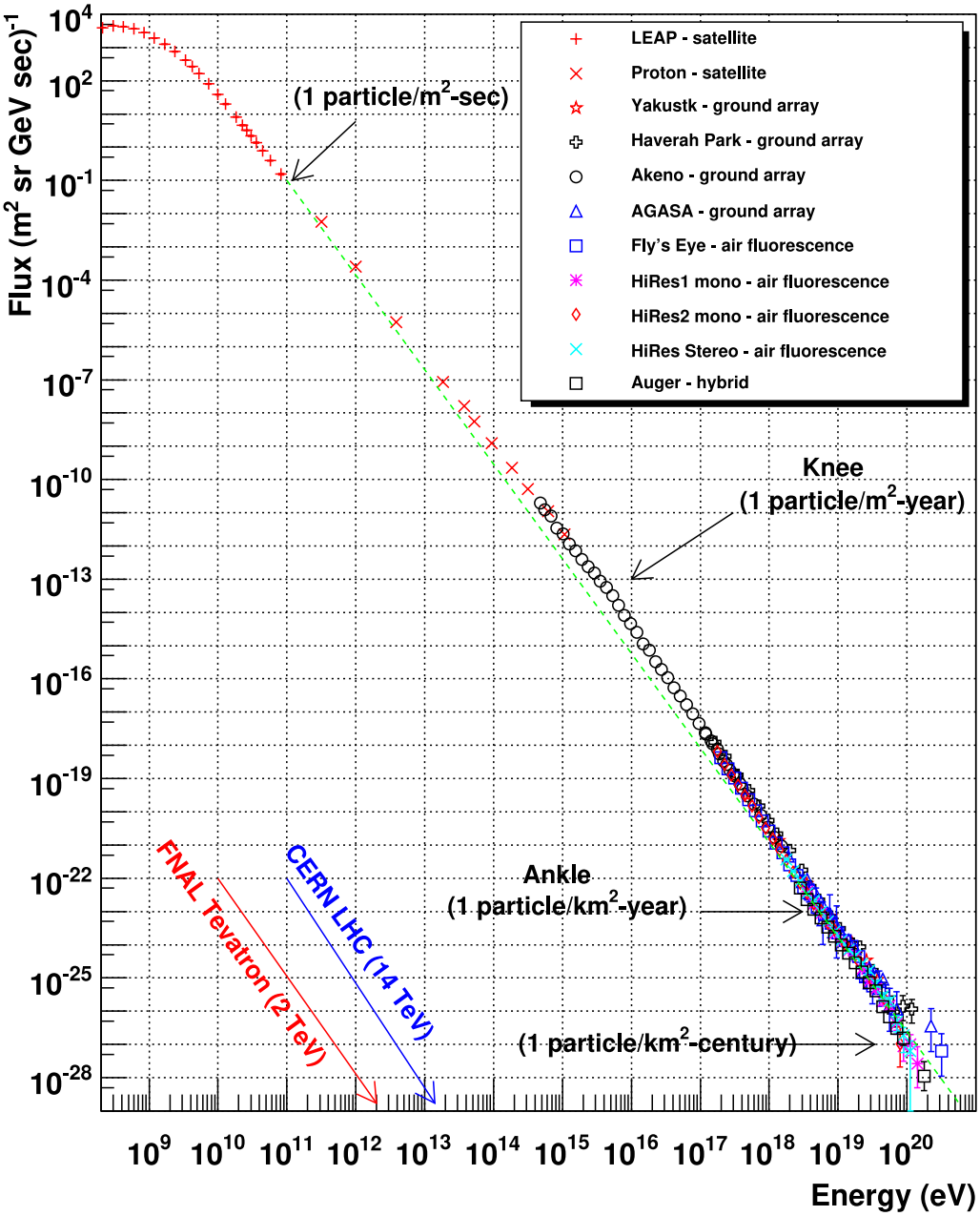


Figure 1.2: Cosmic-ray energy spectrum measured by various experiments. From [20], updated by W. Hanlon.

Another way how the propagation of cosmic rays is influenced is by their interactions with other particles in space and by the loss of their energy. The interstellar space is filled with various types of photon backgrounds, e.g. cosmic microwave background (CMB), which is related to the GZK cutoff, or extragalactic background light (EBL), which includes photons originating e.g. from active galactic nuclei. Interactions of proton primaries with these photon backgrounds cause energy losses in the form of electron-positron pair production or photopion production. Heavier nuclei may in addition to the two mentioned processes undergo photodisintegration or spallation.

## 1.3 Cosmic-ray showers

Cosmic-ray showers are extensive cascades of particles initiated by interactions of high-energy primary cosmic-ray particles with atmospheric nuclei. The number of particles participating in the cosmic-ray shower increases by subsequent interactions of the secondary particles with the atmosphere until a given point, where the energy of the participating particles is insufficient to give rise to new particles. Depending on the initial particle, these showers can be divided into hadronic and electromagnetic. General behaviour and basic properties of each of these two types of showers can be described by simplified models. The two types of extensive air showers are shown in Figure 1.3 and will be described in the following text.

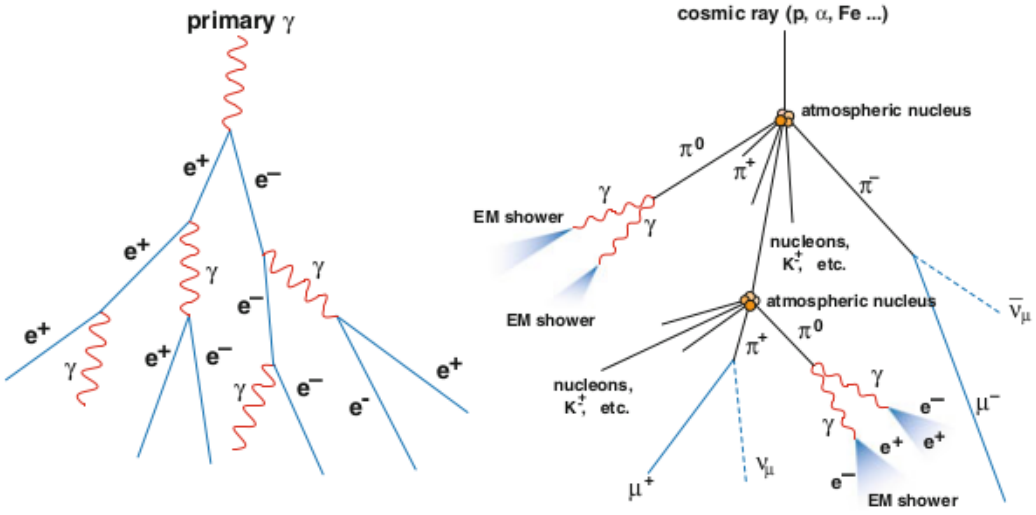


Figure 1.3: Schematic illustration of extensive air showers. *Left:* Electromagnetic shower induced by a photon. *Right:* Hadronic shower induced by a nucleus [22].

### 1.3.1 Development of electromagnetic showers

Electromagnetic showers can be initiated by photons, electrons and positrons. The number of particles in the electromagnetic shower is increased by two basic mechanisms. The first mechanism is the production of electron-positron pair from one photon. The second mechanism is the bremsstrahlung radiating one photon by an electron or a positron. Both of these methods double the number of particles in the shower. In a simplified model, called the Heitler model [23], this doubling of shower participants happens after a given distance that is referred to as the *splitting length*. The splitting length $d$ is defined as

$$d = \lambda_{\mathrm{r}} \cdot \ln 2, \tag{1.4}$$

where $\lambda_r$ is the radiation length of the considered particle in a given medium[3].

Another fundamental feature of the Heitler model is the equal division of energy in each interaction. This means that if the shower is initiated by a photon with an energy $E_0$, the photon will produce, after one splitting length, an electron and a positron with energies $E_0/2$. After another splitting length, both the electron and the positron will radiate one photon and so the shower will contain electron, positron and two photons, all with energies $E_0/4$. This sequence will continue until energies of all particles reach the critical energy $E_c$, at which the ionisation energy loss becomes dominant in comparison with the radiation energy loss[4]. At that point, the number of particles in the shower starts to decrease, defining the stage of shower with the maximal number of particles.

Since after every splitting length the total number of particles in the shower doubles, the number of particles after the $n$-th splitting length will be $N = 2^n$. Moreover, each particle will carry energy $E_n = E_0/2^n$ and the depth traversed by the shower will be $x_n = n\lambda_r \ln 2$. From these assumptions, we can now derive formulas describing the basic properties of the shower simply by taking $n_c$ as the number of splitting lengths needed to reach the critical energy. The maximum number of particles will therefore be given as $N_{max} = 2^{n_c}$, from which it is seen that the initial energy satisfies $E_0 = E_c N_{max}$. Inserting the explicit relation for $N_{max}$ in the formula for initial energy, we get formula for the number of splitting lengths needed to reach the critical energy

$$n_c^\gamma = \frac{\ln\left(\frac{E_0}{E_c}\right)}{\ln 2}, \tag{1.5}$$

where the index $\gamma$ signifies that the formula is relevant for electromagnetic showers.

Using Equation (1.5), we can derive relation for the distance traveled by the shower up to the point with the maximum number of particles. This distance is called the depth of the shower maximum $X^\gamma_{max}$ and the relation is

$$X^\gamma_{max} = \lambda_r \cdot \ln\left(\frac{E_0}{E_c}\right). \tag{1.6}$$

Related to the depth of the shower maximum is the elongation rate $\Lambda$ giving the rate of increase of $X_{max}$ with the decade of primary energy:

$$\Lambda^\gamma = \frac{\mathrm{d}X^\gamma_{max}}{\mathrm{d}\log_{10}(E_0/1\ \mathrm{eV})}. \tag{1.7}$$

By inserting Equation (1.6) into the defining formula for the elongation rate we obtain

$$\Lambda^\gamma = \frac{\lambda_r}{\log_{10}(e)} \approx 2.3 \cdot \lambda_r, \tag{1.8}$$

estimating $\Lambda^\gamma \approx 85$ g/cm$^2$ per decade of primary energy for radiation length of electron in air.

In spite of its simplicity, the Heitler model of electromagnetic showers correctly

[3]The radiation length of electron and positron in air is $\lambda_r^{\text{e-air}} \approx 37$ g/cm$^2$ [24].

[4]The critical energy of electron and positron in air is $E_c^e \approx 85$ MeV [23].

predicts two aspects of these showers: the value of the elongation rate and the dependence of $X^{\gamma}_{\max}$ on the primary energy. On the other hand, one shortcoming is its overestimation of the ratio of electrons to photons.

### 1.3.2 Development of hadronic showers

Hadronic showers can be initiated by neutrons, protons, or heavier nuclei. The interaction of the primary particle with the atmospheric nucleus creates mostly pions ($\tau_{\pi^{+/-}} \approx 2.6 \cdot 10^{-8}$ s, $\tau_{\pi^0} \approx 8.4 \cdot 10^{-17}$ s [25])[5] and to some extent also kaons ($\tau_{\mathrm{K}^{+/-}} \approx 1.2 \cdot 10^{-8}$ s, $\tau_{\mathrm{K}^0_{\mathrm{S}}} \approx 0.9 \cdot 10^{-10}$ s, $\tau_{\mathrm{K}^0_{\mathrm{L}}} \approx 5.1 \cdot 10^{-8}$ s [25]). Charged pions and kaons can then decay into muons and neutrinos travelling to the surface without further interactions, or interact with the atmospheric nuclei producing additional hadrons. Both charged and neutral kaons decay into two or three pions. Neutral pions decay rapidly into two photons that further induce electromagnetic showers.

In analogy to the electromagnetic showers, the development of hadronic showers can be described in a simplified Heitler-Matthews model [26]. One of its fundamental assumptions is the division of the atmosphere into layers of thickness $\lambda_{\mathrm{I}} \ln 2$. The $\lambda_{\mathrm{I}} \approx 120$ g/cm$^2$ is the interaction length of pions with energy 10 GeV – 1 TeV. After passing through one layer, a hadronic particle produces $N_{\mathrm{ch}}$ charged and $\frac{1}{2}N_{\mathrm{ch}}$ neutral pions. Similarly to the Heitler model, energy distribution between new-born particles is considered to be uniform in each interaction. The number of particles participating in the shower development increases until the energy of charged pions falls below the pion critical energy in air $E^{\pi}_{\mathrm{c}} \approx 20$ GeV. At this energy, the decay length of a charged pions becomes smaller than their interaction length and the charged pions start to decay before interacting with other particles.

Since a simplified description of extensive air showers induced by nuclei with $A > 1$, where $A$ is the atomic number of the nucleus, is based on proton-induced showers, the discussion of hadronic-shower properties starts by describing a shower initiated by primary proton with energy $E_0$. After passing an atmospheric depth $X_0$[6], the proton interacts creating $N_{\mathrm{ch}}$ charged pions, each with energy

$$E_{\pi} = \frac{\frac{2}{3} \cdot E_0}{N_{\mathrm{ch}}}. \tag{1.9}$$

After passing $n$ layers, the number of charged pions will be $(N_{\mathrm{ch}})^n$ each carrying energy $\left(\frac{2}{3}\right)^n E_0$. The energy carried by a charged pion in the $n$-th layer is

$$E_{\pi} = \frac{E_0}{\left(\frac{3}{2} \cdot N_{\mathrm{ch}}\right)^n}. \tag{1.10}$$

From this formula, the number of layers $n_{\mathrm{c}}$ needed for the pions to reach their critical energy $E^{\pi}_{\mathrm{c}}$ can be written as

$$n_{\mathrm{c}} = \frac{\ln\left(\frac{E_0}{E^{\pi}_{\mathrm{c}}}\right)}{\ln\left(\frac{3}{2} \cdot N_{\mathrm{ch}}\right)}. \tag{1.11}$$

[5] $\tau$ corresponds to the mean lifetime of the respective particles.

[6] $X_0$ is the depth of the first interaction betweeen the cosmic ray and the atmospheric nuclei.

This quantity can then be used to calculate the number of muons $N_\mu$ in the proton-induced shower. Since muons are products of charged pion decay, their number will be equal to the number of charged pions after $n_c$ layers, that is

$$N_\mu^p = (N_{ch})^{n_c}. \tag{1.12}$$

By employing Equation (1.11), the number of muons can be expressed in the following way

$$\ln N_\mu^p = \frac{\ln\left(\frac{E_0}{E_c^\pi}\right)}{\ln\left(\frac{3}{2}\cdot N_{ch}\right)} \cdot \ln\left(N_{ch}\right) = \beta \cdot \ln\left(\frac{E_0}{E_c^\pi}\right), \quad \beta = \frac{\ln\left(N_{ch}\right)}{\ln\left(\frac{3}{2}\cdot N_{ch}\right)}, \tag{1.13}$$

from which it implies

$$N_\mu^p = \left(\frac{E_0}{E_c^\pi}\right)^\beta. \tag{1.14}$$

Another property that can be explicitly expressed within the Heitler-Matthews model is the primary energy $E_0$. The initial relation is the conservation of energy

$$E_0 = E_c^e \cdot N_{max} + E_c^\pi \cdot N_\mu^p, \tag{1.15}$$

where the first term comes from neutral pions initiating electromagnetic showers and the second term comes from the charged pions. Next step is to rewrite the maximum number of particles in electromagnetic showers as the number of electrons $N_e$. This is accomplished by application of a scaling constant $g$ as $N_{max} = gN_e$. Using this notation, the formula for the primary energy can be written as

$$E_0 = g \cdot E_c^e \cdot \left(N_e + \frac{E_c^\pi}{gE_c^e} \cdot N_\mu^p\right). \tag{1.16}$$

It is thus seen that the primary energy can be estimated from the knowledge of the number of electrons and muons in the proton-induced shower.

The last two aspects of the Heitler-Matthews model that will be described here are the depth of the shower maximum and the elongation rate. The depth of the shower maximum $X_{max}^p$ is estimated from the electromagnetic part of the shower, since it contains the majority of the particles. For more simplicity, the electromagnetic part is taken only from one generation of the neutral pions.

The interaction of a cosmic-ray proton after passing atmospheric depth $X_0$ yields $\frac{1}{2}N_{ch}$ neutral pions decaying into $N_{ch}$ photons. All of these photons then induce electromagnetic showers with primary energies $E_0/(3N_{ch})$. The depth of the shower maximum of these electromagnetic showers is given by the Equation (1.6) and the depth of the shower maximum for primary protons will therefore satisfy equation

$$X_{max}^p = X_0 + \lambda_r \cdot \ln\left(\frac{E_0}{3 \cdot N_{ch} \cdot E_c}\right). \tag{1.17}$$

This equation can be further rewritten by applying fundamental properties of logarithm as

$$X_{max}^p = X_{max}^\gamma + X_0 - \lambda_r \cdot \ln(3 \cdot N_{ch}). \tag{1.18}$$

In analogy with the description of electromagnetic showers, the depth of the shower maximum is used to derive the formula for the elongation rate. Using (1.7), we get

$$\Lambda^{\mathrm{p}} = \frac{\mathrm{d}X^{\mathrm{p}}_{\mathrm{max}}}{\mathrm{d}\log_{10}(E_0/1\ \mathrm{eV})} = \Lambda^{\gamma} + \frac{\mathrm{d}}{\mathrm{d}\log_{10}(E_0/1\ \mathrm{eV})}\left[X_0 - \lambda_{\mathrm{r}} \cdot \ln(3 \cdot N_{\mathrm{ch}})\right]. \quad (1.19)$$

Since the Heitler model already provides the values of $\Lambda^{\gamma}$ and $\lambda_{\mathrm{r}}$, only the dependencies of $X_0$ and $N_{\mathrm{ch}}$ on $E_0$ are needed to evaluate the elongation rate of proton-induced showers. For the estimation of behaviour of $X_0$, the Heitler-Matthews model approximates the interaction length of protons using the results of the measurement of inelastic p-air cross-section from [27]. The number of charged pions produced in one interaction is parametrized from the p-p data from [28]. For the explicit formulas of $X_0$ and $N_{\mathrm{ch}}$, see [26].

With the described estimations, the value of elongation rate for proton-induced showers is $\Lambda^{\mathrm{p}} \approx 58$ g/cm$^2$ per decade of the primary energy. Again, despite the simplicity of the extensive air-shower model, this estimation is comparable with more detailed simulations, see [27]. Moreover, Equation (1.19) indicates the factors reducing the $\Lambda^{\mathrm{p}}$ compared with the $\Lambda^{\gamma}$: an increase of multiplicity associated with the $N_{\mathrm{ch}}$, and a decrease of cross-section associated with the $X_0$.

The last short discussion concerning the hadronic air showers will be focused on showers induced by nuclei with $A > 1$. This type of hadronic showers is described by the so-called Superposition model [29]. The following text is derived from [26] as the Superposition model can be easily built on the Heitler-Matthews model. In this simplified model, the nucleus with atomic number $A$ behaves as $A$ individual nucleons, each with energy $E_0/A$. Derivation of the relevant formulas therefore uses one proton-induced shower with primary energy $E_0/A$ and sums over $A$ showers. The results for the number of muons and depth of the shower maximum are

$$N^{\mathrm{A}}_{\mu} = N^{\mathrm{p}}_{\mu} \cdot A^{0.15}, \quad (1.20)$$

$$X^{\mathrm{A}}_{\mathrm{max}} = X^{\mathrm{p}}_{\mathrm{max}} - \lambda_{\mathrm{r}} \cdot \ln A. \quad (1.21)$$

Especially the result for $X^{\mathrm{A}}_{\mathrm{max}}$ is interesting because it signifies that showers initiated by heavier primaries will reach their maxima traversing less matter, i.e. these showers will have their maximum number of particles at higher altitudes. For example, for iron nuclei ($A = 56$), the $X_{\mathrm{max}}$ will be lower by $\sim$150 g/cm$^2$, which is in good agreement with more detailed simulations, see [30].

## 1.4 Cosmic-ray detection

Detection of cosmic rays can be divided into two groups. The first one is the direct detection of the primary cosmic-ray particle before it hits the atmosphere and the second one is the indirect detection of the primary particle through the induced extensive air shower of secondary particles. From the cosmic-ray energy spectrum (see Figure 1.2) it can be deduced that direct observation of UHECR is practically impossible and cosmic rays with high energies have to be investigated indirectly

from the subsequent air showers.

The main techniques applied to the detection of extensive air showers are arrays of surface detectors measuring particles that travel to the Earth's surface, and telescopes measuring the fluorescence and Cherenkov light emitted by charged particles traversing the atmosphere [3]. The surface detectors can be used for reconstruction of the shower core, the arrival direction of the primary particle or the size of the shower, from which the energy of the primary particle can be estimated. The telescopes can estimate the shower geometry, its longitudinal profile and the arrival time. However, because of the high sensitivity of the fluorescence telescopes, they can effectively operate only on clear, moonless nights decreasing their duty cycle to $\approx$15%.

The largest cosmic-ray shower experiment on our planet is the Pierre Auger Observatory. It is situated in Argentina and it uses both the surface detector array and the fluorescence telescopes for detection of extensive air showers of UHECR. A thorough description of the Pierre Auger Observatory will be provided in the next chapter. Another experiment using both the surface detectors and the telescopes operating nowadays is the Telescope Array. Telescope array is the largest detector of cosmic rays in the Northern hemisphere, being situated in the USA and covering an area of about 800 km$^2$ [3]. It consists of more than 500 surface scintillator detectors and 3 telescope stations, each containing 12 fluorescence telescopes.

One of the experiments that employed only one shower-detection technique is the Karlsruhe Shower Core and Array Detector (KASCADE). KASCADE was a cosmic-ray experiment in Germany that used different types of surface detectors for different components of the shower [31]. For the detection of electromagnetic part of the showers, KASCADE recorded signals from the array of scintillation counters, for the hadronic part a sampling calorimeter and for the muonic part shielded scintillators and tracking chambers. The experiment started to collect data in 1996 and in 2003 it was upgraded to KASCADE-Grande. This upgrade enlarged its area to 0.5 km$^2$ and extended the measurable shower energy range up to $\approx 10^{18}$ eV. Another cosmic-ray experiment located in Karlsruhe was called LOPES [32] and it detected the extensive air showers through the radio emission of the shower particles in frequencies from 40 MHz to 80 MHz. This experiment ran in coincidence with KASCADE-Grande. The KASCADE Collaboration developed the simulation code CORSIKA [33] described in more detail in Chapter 3.

An example of a solely fluorescence-based experiment is the Fly's Eye [34], located in Utah, the precursor of the Telescope Array. This no longer operating experiment consisted of 880 photomultiplier tube (PMT) pixels overlooking the sky. One of its greatest achievements is the detection of a cosmic-ray particle with the highest energy ever recorded. The particle is nowadays referred to as the Oh-My-God particle and its measured energy is $(3.2 \pm 0.9) \cdot 10^{20}$ eV. A successor of the Fly's Eye experiment was the High Resolution Fly's Eye (HiRes) [35] experiment consisting of two sites with 22 (HiRes I) and 42 (HiRes II) telescopes. HiRes was the first experiment to observe the GZK cutoff.

# Chapter 2

# The Pierre Auger Observatory

The Pierre Auger Observatory [36] is located on a high plain near Malargüe in Argentina with the mean altitude of about 1400 m corresponding to the atmospheric depth of $\approx$ 875 g/cm$^2$. Being spread over more than 3000 km$^2$, it is the largest cosmic-ray detector ever built. The first idea of creating such enormous air shower observatory was formulated on the 22$^{\text{nd}}$ International Cosmic Ray Conference in 1991. Four years later, a Science Design Report describing the design and estimated cost was produced. Next step was the evaluation of potential sites for the experiment towards choosing the most appropriate location in the Southern hemisphere. For the validation of the design of the Observatory, a preliminary detector, called the Engineering Array, was build. It was composed of 32 surface array detectors and 2 fluorescence telescopes. By the end of 2001, it was able to observe and reconstruct cosmic-ray showers by combining both detection techniques. Following the successful performance of the Engineering Array, the deployment of final detectors started. Two years later, in January of 2004, the Observatory finally started to collect data and in 2005 the Pierre Auger Collaboration presented the first scientific results.

## 2.1 Hybrid detector

The Pierre Auger Observatory combines two different types of air-shower detection techniques, the fluorescence detector (FD) and the surface detector (SD). The FD is composed of 24 fluorescence telescopes equally distributed over 4 sites. The names of the FD sites are Los Leones, Los Morados, Loma Amarilla and Coihueco. Another part of the FD are the High Elevation Auger Telescopes (HEAT). HEAT includes 3 additional fluorescence telescopes and it is located near the Coihueco site observing the higher-elevation sky to detect showers of lower energies. The SD, overlooked by the FD, is composed of a triangular grid of 1600 water-Cherenkov stations with 1.5 km spacing, distributed over an area of about 3000 km$^2$, and 60 water-Cherenkov stations with spacing of 750 m. This smaller and denser SD array, so-called Infill, is situated near HEAT and these two detectors together lower the energy range of the Observatory down to $10^{17}$ eV. A schematic view of the SD array and the FD of the Pierre Auger Observatory is shown in Figure 2.1.

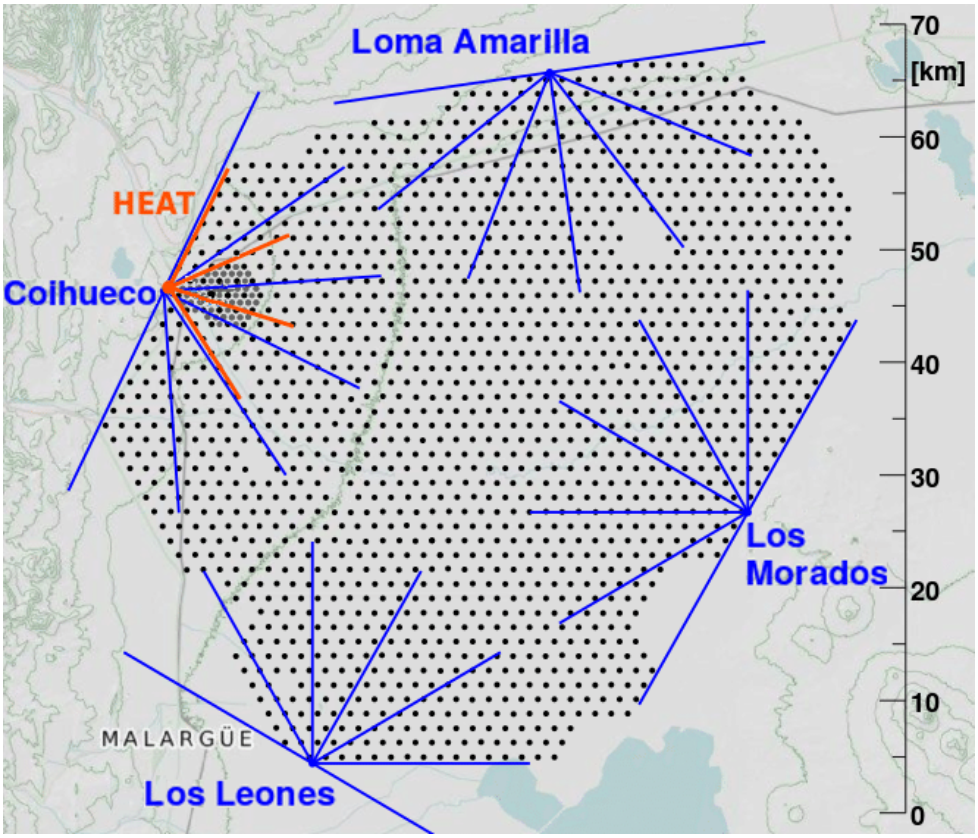


Figure 2.1: Schematic view of the Pierre Auger Observatory with the 1660 SD stations (black dots) and the 4 FD sites (blue) + HEAT (orange) with the azimuthal fields of view of the 27 telescopes (lines) [37].

The water-Cherenkov stations are tanks with diameter of 3.6 m filled with 12000 l of ultra-pure water. Inside each tank, there are three symmetrically distributed PMTs mounted on top of the stations pointing downwards the water volume. The PMTs collect the Cherenkov light emitted in the water by the secondary particles and reflected on the inner surface of the tank. Additional electronic components of each station include a processor, a power controller, a radio transceiver and a GPS receiver. All of these components together with the PMTs are powered by a solar system feeding two lead-acid batteries, and thus making every station self sustainable. One SD station with described components is depicted in Figure 2.2. The SD stations are able to collect data almost 100% of the time, being interrupted only when some part of the station stops working. To prevent a scenario where the Observatory would have more than 20 stations non-operational at the same time, the whole SD array is being continuously monitored, and the stations are under regular maintenance.

Concerning the FD, each of the 24 fluorescence telescopes that are distributed over four sites has a field of view of $30° \times 30°$ in azimuth and elevation with the elevation range starting at 1.5° above the horizon. One site therefore covers 180° in azimuth, as it is seen in Figure 2.1. On the other hand, the 3 High Elevation Auger Telescopes cover the elevation range between 30° and 58° and their total azimuthal field

of view is 120°. The other difference between the 24 telescopes and HEAT are their sampling frequencies. While the classic telescopes have electronics kit that samples with frequency of 10 MHz, HEAT electronics samples with frequency of 20 MHz.

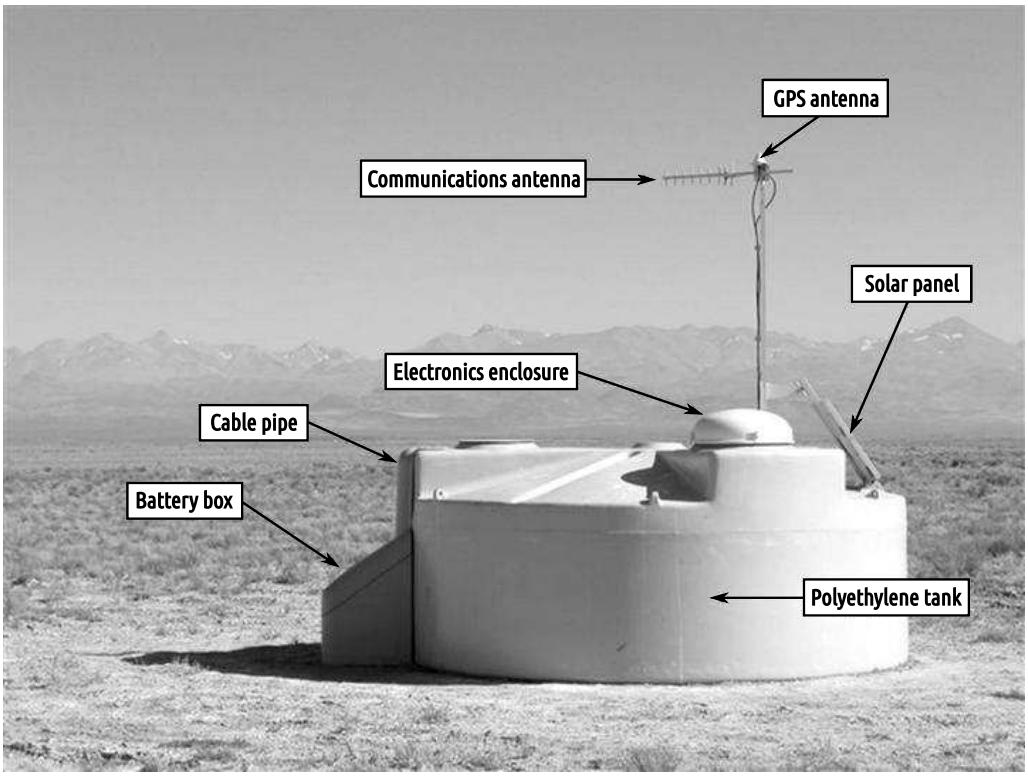


Figure 2.2: Picture of the Pierre Auger Observatory surface detector station with its exterior components described [36].

The fluorescence light coming to one of the telescopes passes at first through a UV filter glass with 1.1 m radius. This filter is responsible for the reduction of background-light flux, resulting in an improvement of the signal-to-noise ratio. After passing the filter, a segmented spherical mirror focuses the light onto a spherical focal surface, from which the signal is collected by a camera. This camera is made up of 440 hexagonal PMT pixels distributed in a $22 \times 20$ grid. Thanks to the filter glass, the rooms with the telescopes and their relevant electronics are kept clean and within controlled climate. Another important component ensuring that each telescope works properly is the shutter. Because of a high sensitivity of the cameras, the telescopes need to be covered during the day and during nights with bad weather conditions, like rain or strong wind. In case of a problematic behaviour of the shutter, an additional security to the camera is provided by a fail-safe curtain. An illustration of the fluorescence telescope with the description of aforementioned components is in Figure 2.3.

Since the FD uses the atmosphere as a medium of calorimeter, the atmospheric conditions have to be monitored for a precise reconstruction of the air showers. Very important is the knowledge of the aerosol content in air. To this end, the Observatory uses two laser facilities that monitor the concentration of the aerosols

in the atmosphere in 15-minute intervals, and four elastic lidars[1], each situated next to a FD site. The laser facilities are called the Central Laser Facility (CLF), and the eXtreme Laser Facility (XLF). In addition to the aerosol measurements, the lidars are also responsible for evaluation of the cloud coverage and cloud height. They operate automatically during the duty cycles of the fluorescence telescopes and scan the sky outside of the FD field of view to not affect the fluorescence light measurements. The measured atmospheric data are then stored in the MySQL[2] databases.

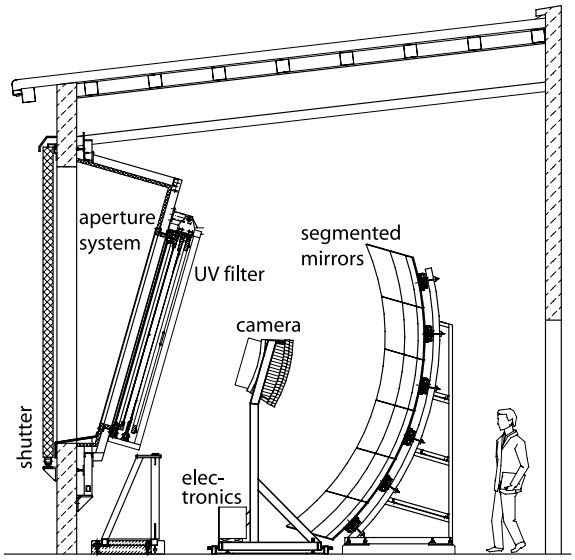


Figure 2.3: Illustration of the Pierre Auger Observatory fluorescence telescope with its most significant components described [36].

The water-Cherenkov station array and the fluorescence telescopes together constitute a hybrid detector of cosmic rays, which is able to simultaneously observe air showers through two different methods. This enables not only to cross-check between the detector stations and the telescopes, but it also provides data with higher quality. The SD itself is not able to measure the longitudinal development of the shower (shower-to-shower fluctuations). Moreover, the signal depends strongly on the detail of hadronic interactions predicted differently by various models of hadronic interactions. The calibration of SD signal using the precise FD measurement of electromagnetic shower component decreases the systematic uncertainty of the SD energy measurement. At the Pierre Auger Observatory, the reconstruction of the shower energy from the SD data is performed from the measured signals in the detectors to estimate a signal at 1000 m from the shower core $S(1000)$.

Besides the two main detection techniques, the Observatory employs the Auger Engineering Radio Array (AERA) for detection of radio emission from air showers. Another additional detector is the Auger Muon and Infilled Ground Array

[1]Lidar shoots short laser pulses and detects the back-scattered light in order to scan the atmosphere and calibrate the shower-energy reconstruction [38].

[2]MySQL is an open-source database system [36].

(AMIGA) consisting of the aforementioned SD Infill and an array of buried scintillators, referred to as the muon detector (MD). AMIGA is devoted to the measurement of the muonic component of air showers. An ongoing upgrade called AugerPrime [39] further introduces new scintillator detectors and radio antennas on top of each water-Cherenkov station with an additional PMT inside. Another part of the Auger upgrade is the new SD electronics. AugerPrime is mainly motivated by the increased ability to distinguish different air-shower components leading to composition-sensitive measurements on event-by-event basis.

For communication between the detectors and the Central data acquisition system (CDAS) located in Malargüe, the Observatory uses a bidirectional radio frequency telecommunication network [36]. The communication includes sending commands to the detectors, receiving data from them, monitoring the detectors or e.g. identifying the event triggers. The communication network itself consists of WLAN and microwave backbone network. The WLAN interconnects individual SD stations and links each of them to one of the four FD sites. The FD sites are then connected together with the center in Malargüe via the microwave backbone network. The detected events that pass through all triggers are sent through the communication network to the CDAS.

## 2.2 The Offline software framework

The Pierre Auger Observatory Offline framework [40], also referred to as Auger Offline, is an interface designed for application of simulation and reconstruction algorithms as well as for development of these algorithms. Furthermore, it provides access to event data and to time-dependent information about detector conditions. Auger Offline is therefore an instrument used for analysis of the Pierre Auger Observatory data. Moreover, parts of its code were also implemented by other cosmic-ray experiments.

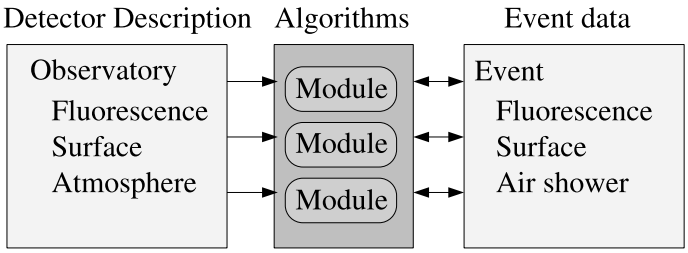


Figure 2.4: General structure of Auger offline. The simulation and reconstruction algorithms are encoded in processing modules having access to the detector description and event information [40].

As it is depicted in Figure 2.4, Auger Offline can be generally divided into three groups: detector description, processing modules and event data. The detector description is responsible for the access to the time-dependent data about detector and atmospheric conditions, and calibration constants. The processing modules are

codes used for individual event-processing tasks. Finally, the event data model provides access to information about events and allows an exchange of data between different modules.

The processing modules are written in C++ and they can be combined together with each other via an XML-based[3] sequencing. Every Auger Offline user can either write a new module or a sequence of already existing modules to create applications based on user requirements. The sequencing instructions are specified and can be edited in an XML file called *ModuleSequence*. By default, Auger Offline already includes many standard applications focused mainly on the reconstruction of different Observatory data (hybrid, AERA, SD only, etc.) or reconstruction of simulated data. An example of such application is a simulation of SD, the sequence of which begins with a module that reads the simulated shower data. The modules generate an event at random position on the SD array, simulate the signal and triggers in the water-Cherenkov stations and finally export the simulated event to an external file. The module sequence can further contain loops repeating given modules a specified number of times.

The event-data model is structured into classes connecting modules to raw, reconstructed, simulated, or calibrated data. At the top of the class hierarchy stands an object called Event that is further divided into FEvent, SEvent, ShowerRecData and ShowerSimData classes. FEvent class retrieves raw data from individual telescopes and their individual PMT pixels, SEvent class retrieves raw data from the SD stations and their PMTs, ShowerRecData class retrieves reconstructed properties from SD and FD, and ShowerSimData retrieves properties of simulated showers. The raw Observatory data are stored in a ROOT format, from which they are read by modules using the aforementioned classes. Each Pierre Auger Observatory event has its individual Auger ID reflecting the date and time of detection. The output of the Auger Offline applications is also written into a ROOT file, specifically in an Advanced Data Summary Tree (ADST) [41]. The ADST file then contains reconstructed shower properties, FD and SD signal and similar relevant information about the reconstructed events.

The contents of the ADST files can be viewed in a graphical user interface (GUI) called Event Browser. In the Event Browser, users can either list through all of the included events or find their desired event by its Auger ID or SD ID. For purposes of this work, it is enough to describe only the main Event Browser features of reconstructed hybrid events. For each reconstructed hybrid event, the Event Browser includes a 2D map of triggered SD stations and lines corresponding to the fluorescence light detected by FD sites. It also includes a 3D map containing the triggered SD stations, reconstructed shower geometry and fluorescence light observed by FD. Furthermore, it includes reconstructed shower properties including the longitudinal profile and observed signal on PMT pixels of each FD site that detected the event and also the shower properties reconstructed from the SD signal. Exemplary contents of the Event Browser are shown in Figure 2.5 (2D map of triggered SD stations) and Figure 2.6 (triggered florescence telescope pixels).

The detector description serves as an interface connecting modules to detector configuration and monitoring and calibration data at specified date and time. This

[3]XML stands for Extensible Markup Language.

interface consists of hierarchy of classes similar to the event data model, which can request specific data from so-called managers. Every manager is used to extract specific information from a single data source. These data sources consist of the MySQL databases, which contain atmospheric conditions and other time-varying data from monitoring and calibration, and XML files, which contain time-independent detector information. Additional feature of the detector description are so-called models, which are functions that can be used to process the detector data before their retrieval from the managers. A simple example of this feature is a model that calculates attenuation of light due to aerosols between two points in the atmosphere from atmospheric conditions.

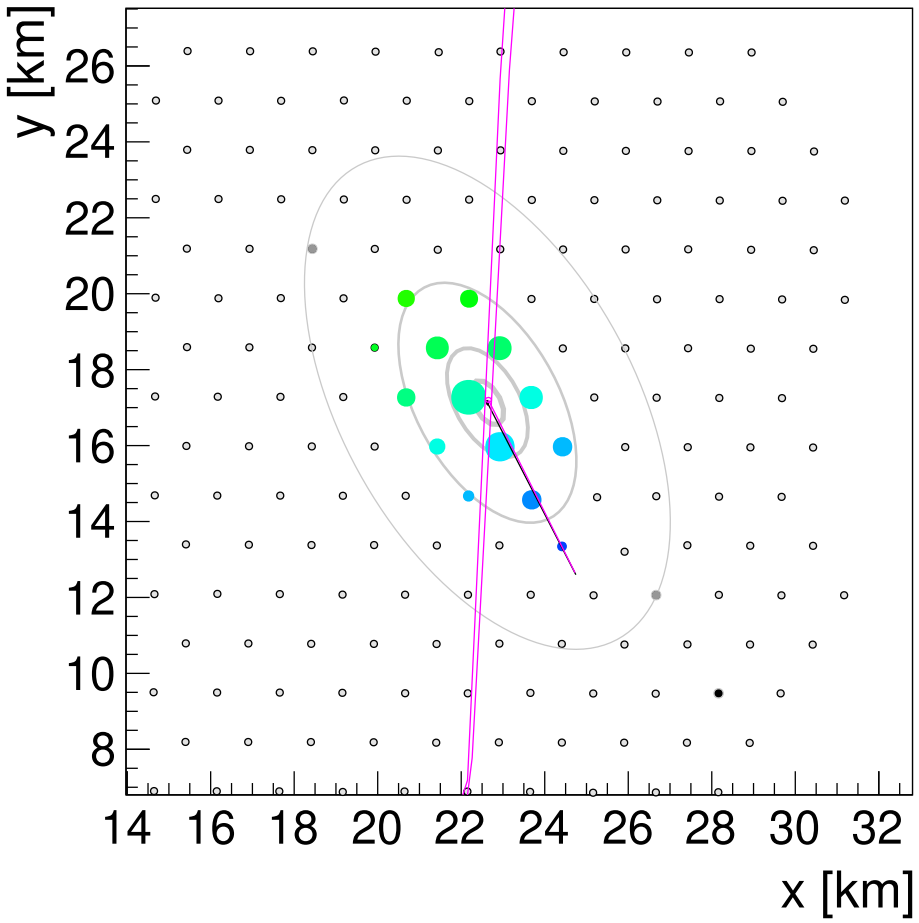


Figure 2.5: Reconstructed Pierre Auger Observatory event with Auger ID 121725991300. 2D map of SD stations in the Observatory coordinate system. Colored points indicate the SD stations triggered by a cosmic-ray shower. Different sizes of the colored points correspond to the size of the signal and different colors to the time sequence of the signals. Long magenta lines correspond to the angular uncertainty of the shower core estimation observed by Los Morados FD site. Short purple line corresponds to the shower axis reconstructed from the FD signal. Produced via Event Browser.

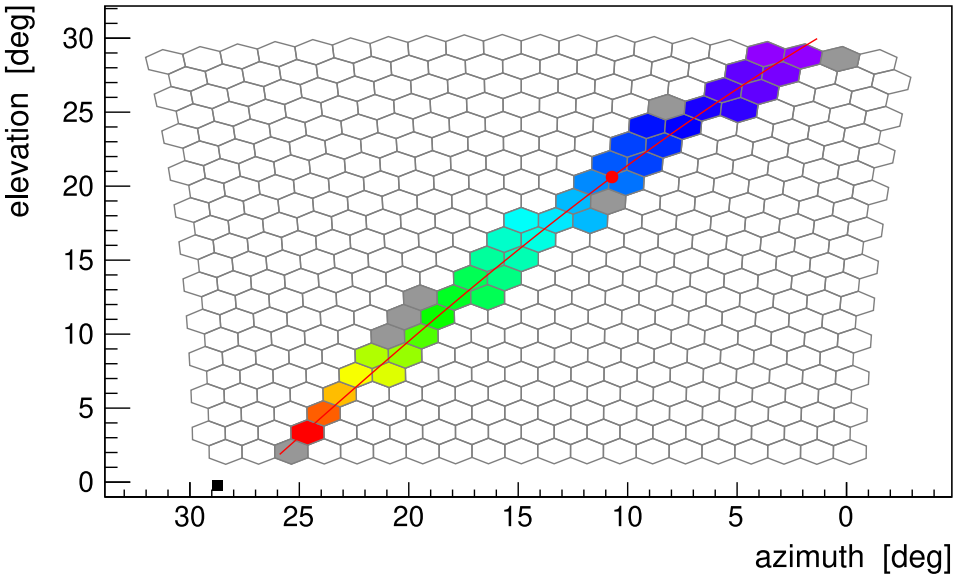


Figure 2.6: Reconstructed Pierre Auger Observatory event with Auger ID 121725991300. Detected signal on PMT pixels of one of the Los Morados fluorescence telescopes. Different colours of the pixels correspond to different incoming times of the fluorescence light. The red line corresponds to the reconstructed trajectory of the shower and the red dot represents the reconstructed $X_{\max}$. Produced via Event Browser.

# Chapter 3

# Simulation of cosmic-ray showers

Extensive air-shower simulations are a vital part of cosmic-ray studies as detailed theoretical predictions allow us to correctly interpret the observed data or to build effective cosmic-ray shower detectors. For the description of the cascade development itself, the simulation codes apply the Monte Carlo (MC) method. However, as the MC shower simulation alone requires a lot of computing time, the codes usually combine it with some other method. For example, a simulation code called CONEX [42] uses MC simulations for the highest-energy part of the shower and numerical solutions of cascade equations for the lower-energy part. A simulation code called CORSIKA [33], on the other hand, can describe the lower-energy part of the shower using the so-called thin sampling [43], described in more detail later in this chapter. The description of hadronic interactions of the shower particles is not built in the MC simulation codes, but it is implemented through the hadronic interaction models as external inputs.

## 3.1 Hadronic interaction models

Although the Heitler-Matthews model of hadronic cosmic-ray showers, described in the first chapter, is able to outline the basic shower development, it is too simple for usage in thorough simulations of extensive air showers. The standard generators of hadronic interactions are implemented in more detail based on the MC method [44]. The advantage of MC is its ability to implement various theoretical models and compare their results with experimental data. The biggest challenge for the hadronic interaction models is undoubtedly the need to describe hadronic collisions at energies much higher than those achieved at particle colliders. To this end, the models are calibrated on available collider data and extrapolated to higher energies.

The widely used high-energy hadronic interaction models in the cosmic-ray shower simulations are QGSJET [45], SIBYLL [46] and EPOS [47]. All of these models are based on the Reggeon Field Theory (RFT) [48] describing high-energy scattering of strongly interacting particles with the use of complex angular momentum. The practical advantage of RFT is its treatment of hadron-hadron collisions as multiple scattering processes. Although the general framework of the models is similar, their

predictions differ because of their individual approaches to the RFT. Differences between the mentioned models can be seen in Figure 3.1, showing dependence of the mean $X_{\mathrm{max}}$ on energy of the primary particle. The data plotted in this figure suggest a shift in the cosmic-ray mass spectrum towards heavier elements with increasing energy assuming that the hadronic interaction models approximate the processes in the atmospheric showers at the highest energies correctly.

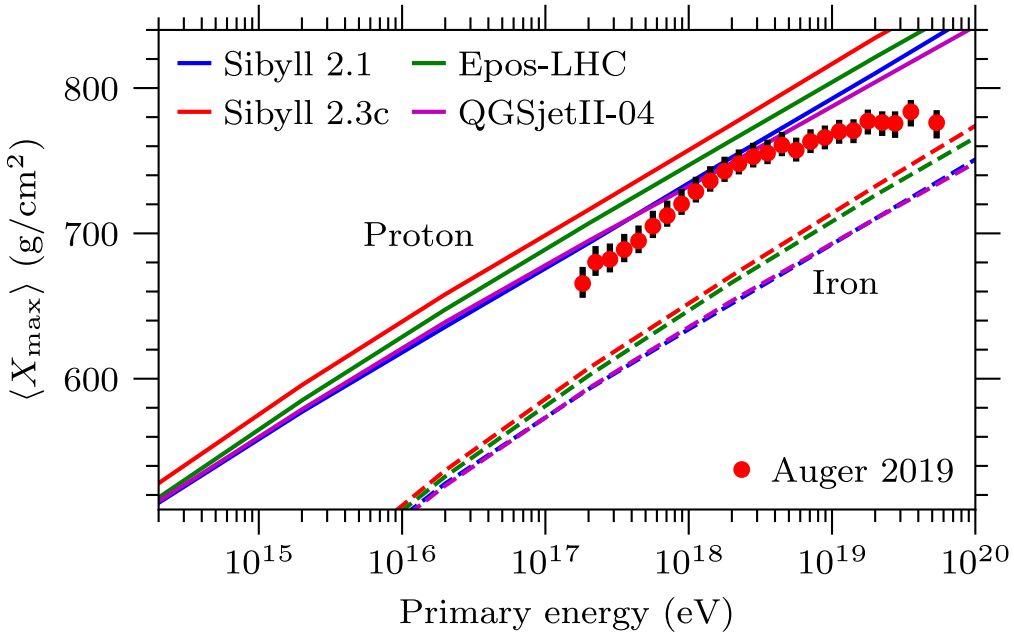


Figure 3.1: Dependence of the mean $X_{\mathrm{max}}$ on primary energy simulated with four different hadronic interaction models for two different primary particle types in comparison with the Pierre Auger Observatory data [49].

QGSJET-II is an improved version of original QGSJET generator [50] simulating hadronic interactions in the framework of quark-gluon string model [51]. The quark-gluon string model is an extension of general RFT by a hadronization model describing each process of elementary particle production by creation of two strings [45]. Thanks to its approach, the original QGSJET model is able to describe high-energy behaviour of scattering amplitudes as the perturbative QCD evolution. This provides the model with a reasonable predictive power. However, this model treats re-scattering processes as independent on each other and thus neglects non-linear effects significant for high parton densities, i.e. in high-energy limit or for small impact parameters.

The QGSJET-II model was designed to take the mentioned non-linear effects into account and to better describe the available data from fixed-target experiments. These improvements led to a reduction of inelasticity and multiplicity of hadron-air collisions in comparison with the original model. This reduction in turn implies lower production rate of secondary particles in cosmic-ray showers implying an increase of the $X_{\mathrm{max}}$. Another changes include the increase of the electron number at sea level that is correlated with $X_{\mathrm{max}}$, and the decrease of the number of muons.

SIBYLL is one of the oldest MC generators of hadronic interactions with its first version dating back to 1987. Its main ideas are based on the minijet model [52–55]

with hadron-air interactions being described by the Glauber model [56]. Interactions of nuclei with the atmosphere are then modeled using a similar approach as the Superposition model that was described in the first chapter [49]. Older versions of SIBYLL predicted much lower numbers of muons in the cosmic-ray showers in comparison with the Pierre Auger Observatory and the Telescope Array data. An update, labeled 2.3d, that improved mainly the leading particle description increased the generated number of muons by 20% - 50%. With this increase, the generator SIBYLL 2.3d predicts the largest number of muons in comparison with other hadronic interaction models.

Finally, EPOS is a newer model describing particle production through the so-called parton ladders and remnant excitation of projectile and target hadrons [57]. Its name is an abbreviation of Energy conserving quantum-mechanical multiple scattering approach based on Partons, Off-shell remnants and Splitting parton ladders. The version of this model nowadays used in the simulations of cosmic-ray showers is called EPOS LHC [58] and it was developed to be consistent with the LHC data from p-p, Pb-p and Pb-Pb scatterings. In comparison with the QGSJET-II version 04, EPOS LHC generates more muons [59], but with a lower average energy. This results in lower invisible energy being generated by the EPOS LHC.

This section serves as a brief introduction to the high-energy hadronic interaction models used in cosmic-ray shower simulators. A detailed description of RFT and other mechanisms mentioned is far beyond the scope of this work. For more information about these topics see e.g. [48, 51, 53] or [60].

## 3.2 CORSIKA

As it is implied by the full name COsmic Ray SImulations for KAscade, the MC extensive air shower simulator CORSIKA was originally developed for the experiment KASCADE [33]. Nowadays, this simulation code is being used by many cosmic-ray experiments including the Pierre Auger Observatory. It is used to predict not only the average values of the shower observables, but also their fluctuations. The code is able to track all secondary particles from the moment of their creation to their decay or interaction and to employ the detailed hadronic interaction models. For simulation of electromagnetic interactions and propagation of electrons and photons, CORSIKA uses modified EGS4[1] system [61] and analytical NKG (Nishimura-Kamata-Graisen) formulas [62, 63].

The simulation of showers through MC alone is unpractical especially for high-energy cosmic rays because the computing time rises almost linearly with the primary energy. To reduce the computing time needed for high-energy shower simulations, CORSIKA introduces the so-called thin sampling, also known as Hillas thinning [43]. The thinning is initiated at a regulable thinning energy $E_{\mathrm{th}}$ and it simplifies the simulations by reducing the number of tracked particles. When energies of secondary particles fall below $E_{\mathrm{th}}$, one of these particles is chosen randomly

[1] EGS stands for the Electron-Gamma Shower.

with the probability

$$p_i = \frac{E_i}{\sum_j E_j}, \tag{3.1}$$

where $E_i$ corresponds to the energy of the selected particle and $E_j$ are energies of the other considered secondary particles. The selected particle is then the only one that remains to be tracked, while the other considered particles are removed from the simulation process. For conservation of the energy, the selected particle is weighted by a factor $w_i = 1/p_i$. In case that not all of the secondary particles have their energy lower than $E_{\text{th}}$ when the thinning is initiated, such particles will survive the process with probability

$$p_k = \frac{E_k}{E_{\text{th}}}, \tag{3.2}$$

and they will also be given a weight factor $w_k = 1/p_k$.

Upon initiation, CORSIKA allows the user to set a number of parameters like the primary particle type, its energy and angle of incidence, atmospheric conditions, model of hadronic interactions or for example the thinning energy. The primary particle can be chosen from any lepton or antilepton including neutrinos, many different hadrons including their corresponding anti-particles and resonances, photons and nuclei up to iron. The primary energy can be either set to a fixed value or a range of energies can be specified, from which CORSIKA selects random values according to a given spectral index. The choice of angle of incidence works in a similar way.

By default, CORSIKA writes two output files. One is the control printout containing a text file describing the code version, input parameters, information about the simulation itself, etc. The second default output is the particle and Cherenkov photon output including all the simulated particles that reached the observable levels. An optional CORSIKA output relevant for this work is a .long file containing longitudinal profile of the particles and deposited energy.

This brief description of the simulation software CORSIKA serves as a clarification of the terms that are relevant for the analysis made in this work. For more detailed information about CORSIKA see, e.g., [33].

# Chapter 4

# Shower reconstruction at the Pierre Auger Observatory

## 4.1 Longitudinal profile

Cosmic-ray showers are the main tool for cosmic-ray particle detection and analysis at energies above $\approx 10^{14}$ eV. In the context of cosmic-ray shower reconstruction, the most important part is played by the longitudinal profile of the cascade. That is because from its correct reconstruction one can obtain the depth of the shower maximum $X_{\max}$ and the calorimetric energy of the shower $E_{\text{cal}}$, from which the energy of the primary particle can be precisely estimated.

The longitudinal profile itself can be defined as the energy deposited by the secondary air-shower particles as a function of the traversed air mass [64]. This air mass is also known as the slant depth $X$ and it is defined by the formula

$$X(z) = \int_z^{+\infty} \rho(x)\mathrm{d}x, \tag{4.1}$$

where $\rho(z)$ is the air density at point $z$. $z$ is the longitudinal coordinate along the shower axis, where the shower axis is defined as the direction from which the primary particle hits the atmosphere. Specifically for shower axis perpendicular to the surface, the coordinate $z$ corresponds to the altitude. The point in the longitudinal profile with the largest energy deposit was already introduced and it is the depth of the shower maximum $X_{\max}$.

Other important terms connected with the longitudinal profile and the shower reconstruction are the shower core and the zenith and azimuth angles. The intersection of the shower axis with the Earth's surface is called the shower core. The zenith and azimuth angles are generally the angles with which the position of some object in the sky can be described. In the context of cosmic-rays, the zenith and azimuth angles can give us the direction from which the primary particle hit the atmosphere, in other words, the direction of the shower axis. Zenith angle is defined as an angle between the direction of the object you want to describe and the line connecting the surface with the zenith. Especially for the case of cosmic-ray showers, the zenith angle is an angle between the shower axis and the line that crosses the shower core

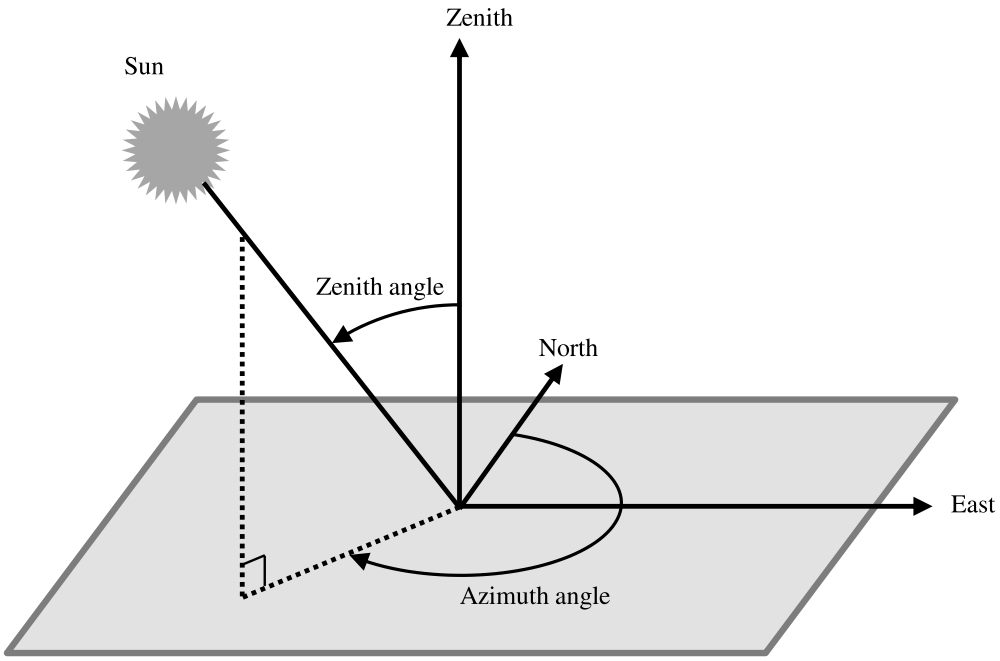


Figure 4.1: Illustration of zenith and azimuth angles used for measurement of the position of the Sun [65].

and is perpendicular to the Earth's surface. For cosmic-ray showers, the azimuth angle is an angle between the northern direction and the projection of the shower axis to the surface plane. A clear illustration of the zenith and azimuth angles for better understanding is in Figure 4.1.

Experimental estimation of the longitudinal profile can be done by measuring fluorescence light emitted by the shower particles. Most of this emitted light is consequence of ionisation by electrons and positrons [64]. A more detailed description of the detection of the fluorescence light and of other methods of the cosmic-ray detection will be provided in the following chapters.

The longitudinal profile can be described by the Gaisser-Hillas function [66]

$$f_{\mathrm{GH}}(X) = \left(\frac{\mathrm{d}E}{\mathrm{d}X}\right)_{\mathrm{max}} \cdot \left(\frac{X - X_0}{X_{\mathrm{max}} - X_0}\right)^{\frac{X_{\mathrm{max}} - X_0}{\lambda}} \cdot e^{\frac{X_{\mathrm{max}} - X}{\lambda}}, \tag{4.2}$$

where $\left(\frac{\mathrm{d}E}{\mathrm{d}X}\right)_{\mathrm{max}}$ is the energy deposited at the depth of the shower maximum and $X_0$ and $\lambda$ are parameters affecting the shape of the function. The measured energy deposit as a function of the slant depth can then be fitted by the Equation (4.2) providing the depth of the shower maximum $X_{\mathrm{max}}$.[1] An example of a measured longitudinal profile fitted by the Gaisser-Hillas function can be seen in Figure 4.2.

[1] In practice, the Gaisser-Hillas function (4.2) is not the only formula used to describe the longitudinal profile. An example of alternative formula is the so-called universal shower profile function.

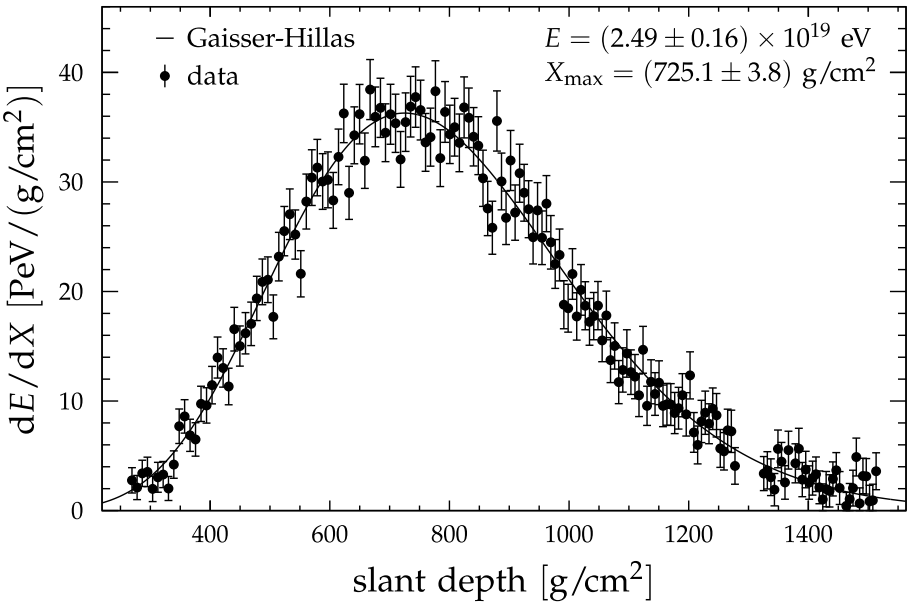


Figure 4.2: Measured longitudinal profile of a cosmic-ray air shower fitted by Gaisser-Hillas function (4.2) with obtained depth of the shower maximum $X_{\max}$ and reconstructed total energy of the shower $E$ [64].

By integrating the formula (4.2) over the whole slant depth of the shower, the energy deposited by the shower is obtained. To get the total energy of the primary particle that initiated the shower, this deposited energy must be added up with the so-called invisible energy that is all the energy that is not deposited in the atmosphere. This includes the energy carried away by particles that do not deposit all of their energy in the atmosphere and also particles that do not interact in the atmosphere at all. Particles that carry the invisible energy are mostly muons and neutrinos.

## 4.2 Standard reconstruction of hybrid events

The standard reconstruction of hybrid events within the Offline framework, also referred to as hybrid data (HD) reconstruction, begins with a few SD pre-selection modules. These modules check if the PMT signal in triggered SD stations has good quality (*SdPMTqualityCheckerKG*), find time delays between different triggers (*TriggerTimeCorrection*), apply these time shifts and reject bad stations based on their calibration data (*SdCalibratorOG*), correct the time offset arising from incorrect position of the SD stations (*SdStationPositionCorrection*), reject specific stations for predefined periods (*SdBadStationRejectorKG*) and recover the saturated signals (*SdSignalRecoveryKLT*).

The set of the SD pre-selection modules is followed by the FD hybrid reconstruction modules. The FD reconstruction begins with calibration of the fluorescence telescopes (*FdCalibratorOG*) and combination of data from HEAT and Coihueco telescopes into the so-called HECO (*FdEyeMergerKG*). In the next step, the telescope

PMT pixels belonging to the observed shower are identified (*FdPulseFinderOG*) and fitted to reconstruct a plane containing the shower axis and the triggered PMT pixels (*FdSDPFinderOG*). This plane is called the shower-detector plane (SDP) and it can be used to define important parameters related to the shower geometry. One of these parameters is the telescope viewing angle $\chi$. This is an angle within the SDP between the ground and the line of sight from which fluorescence photons reached the telescope. Another important parameter is the distance between the telescope and the point of the closest approach of the observed shower axis. This distance is labeled as $R_\mathrm{p}$. More parameters related to the shower geometry as well as the SDP are visualized and defined in Figure 4.3.

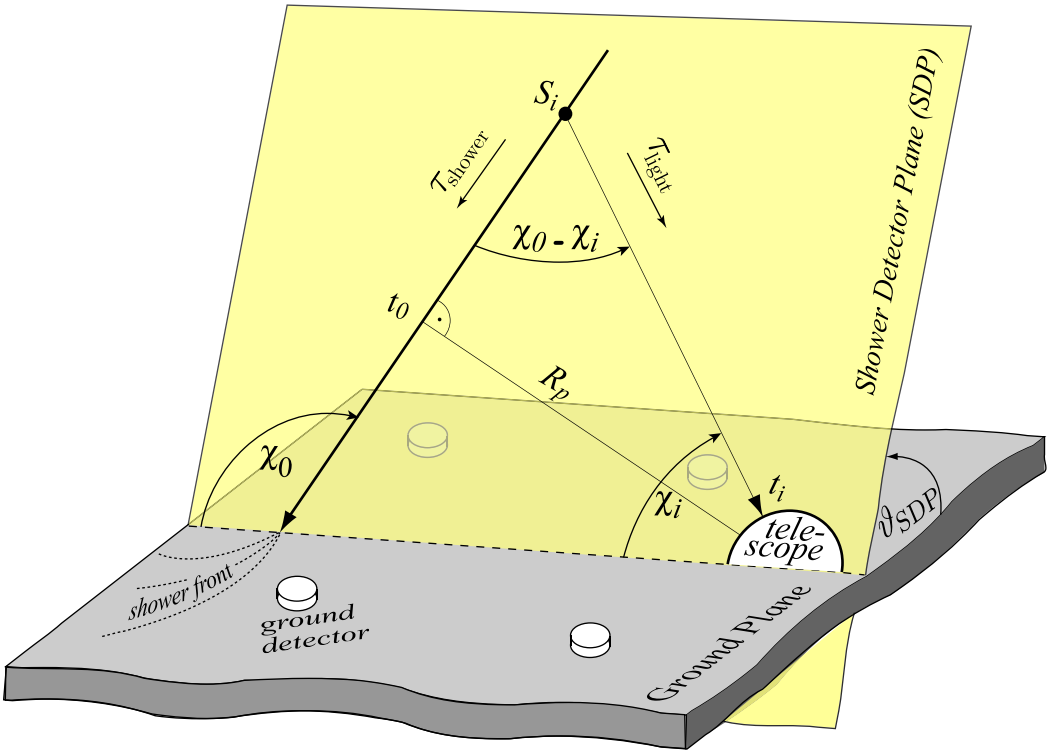


Figure 4.3: Visualization of the shower geometry obtained from the fluorescence telescope. The depicted parameters are the time $t_0$ of the closest approach of the shower axis to the telescope, distance $R_p$ between the shower axis and the telescope at $t_0$, shower propagation time $\tau_{\mathrm{shower}}$ from the point $S_i$ to the point at time $t_0$, light propagation time $\tau_{\mathrm{light}}$ from the point $S_i$ to the telescope, the arrival time $t_i$ of the photons detected by the camera pixel $i$, angle of incidence of the shower axis within the SDP $\chi_0$, viewing angle of pixel $i$ within the SDP $\chi_i$ and the angle of incidence of the SDP $\vartheta_{\mathrm{SDP}}$ [67].

After the determination of the SDP, the algorithm reconstructs the orientation of the shower axis within this plane using arrival times of the photons on individual PMT pixels (*FdAxisFinderOG*). Next, the hybrid shower geometry is reconstructed using all of the FD signal together with the signal from SD station closest to the shower core (*HybridGeometrFinderOG*).[2] Then, the dependence of the total light

[2]For cosmic rays with energies above 3 EeV, the hybrid geometry reconstruction determines the arrival direction of the particles with precision of about 0.5° [68].

flux detected by the telescope on time is calculated from the FD signals (*FdApertureLightKG*). Different bins of this time trace are then projected to their relevant path lengths along the shower axis $\Delta l_i$. Each of these path lengths is then assigned to its appropriate slant depth and height. Then, the amount of light emitted by the shower particles along the $\Delta l_i$ is estimated using the calculated distance between the shower axis and the telescope. From these estimates along the whole observed part of the shower axis, the longitudinal profile of shower can be reconstructed since the produced light is related to the deposited energy.

In the last module of the FD hybrid reconstruction, the produced light profile converted to energy deposit is fitted by the Gaisser-Hillas function (4.2) and the calorimetric energy of the shower and its $X_{\max}$ are obtained (*FdEnergyDepositFinderKG*). The parameters $X_0$ and $\lambda$ are constrained by a Gaussian constraint using the mean and variance estimated from the high quality measured data. These distributions of $X_0$ and $\lambda$ are obtained by applying an unconstrained Gaisser-Hillas fit to a group of events, where the more complex fit is possible. After determining the calorimetric energy, the total energy of the shower, being equal to the energy of the incoming cosmic ray, is inferred by taking into account the invisible energy of the shower. The invisible energy is estimated through its parametrization as a function of the calorimetric energy obtained from measured data [69].

After running the FD hybrid reconstruction modules, the SD reconstruction begins with selection of stations that passed the pre-selection modules without being flagged as bad (*SdEventSelectorOG*). Then, the shower core and the SD shower plane are estimated (*SdPlaneFitOG*). The shower core position is estimated as a signal-weighted barycenter of the selected stations. The SD shower plane is defined as the plane perpendicular to the shower axis that moves together with the shower. The next step is application of the LDF fit to fix the shower core position and estimate the signal measured in detectors 1000 m away from the shower core $S(1000)$ (*LDFFinderKG*). The $S(1000)$ is then used for the shower energy calculation[3] (*EnergyCalculationPG*). The remaining modules are used to calculate the rise time of the event (*Risetime1000LLL*), apply correction for cases when a station PMT captures a whole beam of Cherenkov photons (*DLECorrectionGG*) and, finally, evaluate the SD station triggers (*SdEventPosteriorSelectorOG*).

## 4.3 Reconstruction of hybrid events using the SD geometry

The reconstruction of hybrid events using the SD geometry is an alternative method of the hybrid event reconstruction. Its main difference in comparison with the HD reconstruction is the usage of full SD reconstruction for the shower geometry estimation. This change is implemented into the algorithm via a module called *SdToFdGeometryInjector* replacing the *FdSDPFinderOG*, *FdAxisFinderOG* and *HybridGeometryFinderOG* modules in the FD reconstruction part of the *ModuleSequence*.

The whole structure of the *ModuleSequence* itself is as follows. Just as in the

[3]The shower energy calculated from the FD signal and from the SD signal is stored separately in the output ADST.

case of the HD reconstruction, the FD reconstruction with the use of SD geometry starts with the FD pre-selection modules. These modules remain exactly the same as in the case of the previously described method. After that the SD reconstruction modules follow. Here, the SD reconstruction must be applied before the FD one, because the *SdToFdGeometryInjector* module needs the SD reconstructed data for the input. Just like in the case of the previous method, this method uses the *SdEventSelectorOG*, *SdPlaneFitOG*, *LDFFinderKG*, *EnergyCalculationPG*, *Risetime1000LLL* and *SdEventPosteriorSelectorOG*.

The FD reconstruction begins again with the calibration of the telescopes followed by the identification of the telescope pixels belonging to the observed event. Here, the *FdEyeMergerKG* is omitted. In addition to the standard FD reconstruction, this method uses a module to select only the triggered pixels that are not isolated (*PixelSelectorOG*). Then, the shower geometry is injected through the *SdToFdGeometryInjector* module to further calculate and fit the longitudinal profile.

## 4.4 Stereo reconstruction of FD events

The stereo reconstruction is an alternative method of reconstruction of showers that are detected by more than one FD site. As the name of the method suggests, such showers are referred to as stereo showers. This method uses FD signal only, making it possible to reconstruct showers that did not fall directly onto the SD array.

After reading the input files, the reconstruction begins with a check if the event is reconstructable (*EventCheckerOG*). An example of unacceptable event could be an event with missing detector description. Then, the reconstruction continues with the calibration of the FD, selection of pixels belonging to the event, estimation of the SDP and shower axis processed through the same modules that are employed in the HD reconstruction. The estimation of the geometry can be performed in two ways in this reconstruction method, either with, or without the use of hybrid geometry estimation module. The method relevant for our analysis is the stereo geometry reconstruction alone, performed through a *StereoGeometryFinderOG* module. This module reconstructs the shower axis by finding the best fitting axis from the combination of time-fit and SDP-fit $\chi^2$-functions from each FD site that observed the respective event. After the estimation of the shower geometry, the reconstruction proceeds with the longitudinal profile calculation through the *FdApertureLightOG* module. The longitudinal profile is then fitted by the *FdProfileReconstructorKG* module.

## 4.5 Processing of CORSIKA showers

For the reconstruction of simulated showers, the processing algorithm first needs to generate extensive air showers and detector responses from the CORSIKA output data. At the beginning, the *EventFileReaderOG* module[4] needs to be set to read

[4]This module, together with the basic setup of the Offline reconstruction, is described in Appendix A

the CORSIKA output files. The CORSIKA output files used for the simulation reconstruction in Offline are the .part files with information about particles at the pre-defined ground level and the .long file with the longitudinal profile data. When the input files are loaded, the processing algorithm checks if the MC-reconstructed shower has negative number of entries in its electron profile (*MCShowerCheckerOG*). If that is the case, the input shower in question is skipped, because the shower simulation is faulty, and the next event is processed. After passing the check, the event time and the shower core of simulated shower are generated (*EventGeneratorOG*).

When the generated shower is placed on the Pierre Auger Observatory detector plane, the simulation of the SD signal begins with injecting the simulated particles into the SD stations near the generated shower axis (*CachedShowerRegeneratorOG*). Then, the appropriate stations are simulated using the Geant4-based code [70] used to generate the traversing of particles through the detector medium (*G4StationSimulatorOG*). The simulated detector calibration constants are then saved (*SdSimulationCalibrationFillerOG*) and the signal in the PMTs is generated from the pulses produced through the tank simulation (*SdPMTSimulatorOG*). After that, the SD simulation generates the response of the SD electronics (*SdFilterFADCSimulatorMTU* and *SdBaselineSimulatorOG*), the local station triggers (*TankTriggerSimulatorOG*) and, finally, the station GPS data (*TankGPSSimulatorOG*).

The SD response simulation is followed by generation of the FD signal. This part begins with the calculation of the visible fields of view of all telescopes (*FieldOfViewCalculatorKG*). Then, the telescopes passing some preliminary cuts are accepted (*FdSimEventCheckerOG*), the fluorescence and Cherenkov light produced along the shower axis is simulated (*ShowerLightSimulatorKG*), and the light flux at the accepted FD telescopes is generated (*LightAtDiaphragmSimulatorKG*). The next modules simulate the lateral distribution of the shower (*ShowerPhotonGeneratorOG*), the signal and background in PMTs (*TelescopeSimulatorKG* and *FdBackgroundSimulatorOG*), the response of the FD electronics (*FdElectronicsSimulatorOG*) and, finally, the FD triggers (*FdTriggerSimulatorOG*).

When the SD and FD signal is generated, the processing follows with the simulation of the response of the central data acquisition system to the detector triggers (*CentralTriggerSimulatorXb*). Coincident SD and FD triggers are then used for creation of hybrid event (*CentralTriggerEventBuilderOG*). All of the generated data so far are then combined to create a standard Offline event (*EventBuilderOG*) to be exported into an external file (*EventFileExporterOG*). This event file can then be used as an input file for the *EventFileReaderOG* module.

The reconstruction itself then starts with the *EventCheckerOG* module and calibrations of the FD and the SD. These modules are followed by the FD hybrid reconstruction described above followed by the SD reconstruction. The latter part contains the previously described *SdEventSelectorOG*, *SdSignalRecoveryKLT*, *SdPlaneFitOG*, *LDFFinderKG*, *Risetime1000LLL* and *SdEventPosteriorSelectorOG* modules. Moreover, this SD reconstruction part includes an additional selection module for identification of artificial stations around 1000 m from the shower core that are not used in the shower reconstruction (*SdMonteCarloEventSelectorOG*). With this the reconstruction of the simulated shower ends, and the *RecDataWriterNG* module is called.

# Chapter 5

# Combination of the reconstruction methods using CORSIKA simulations

To be able to combine the results from the HD reconstruction with the reconstruction using the SD geometry or with the FD stereo reconstruction, one needs to study the differences between the systematic uncertainties of the different methods and minimize the biases between them. This minimization of biases can be accomplished either by a study on simulated showers and comparison of the reconstructed properties with the true MC generated properties, or by comparison of identical events reconstructed using the different methods.

In this chapter, we analyse the differences between the standardly used HD reconstruction method and each of the alternative shower reconstruction methods using proton showers with energies between $10^{19.5}$ eV and $10^{20}$ eV and zenith angles within 60° simulated with the CORSIKA 7.5700 code applying the hadronic interaction model EPOS-LHC. The simulated showers were produced by Prague Auger Group as a part of the official simulation library for the Pierre Auger Collaboration. These simulated showers were then processed using the reconstruction sequence described in Chapter 4 performed via the Offline SVN trunk version 34510. Here, the *EventFileExporterOG* module was used to generate exactly the same input files for all of the three analysed methods.

The HD reconstructed simulations and simulations reconstructed using the SD geometry were processed through the sets of $X_{\max}$ and SD cuts described in Appendix A. The stereo-reconstructed data were processed only through the set of $X_{\max}$ cuts as this reconstruction method does not use the SD signal for shower reconstruction at all. The cuts focusing on the atmosphere and hardware status of the detectors were omitted, since the simulated showers do not have any atmospheric information and the generation of the signal in detectors is not based on the time-dependent detector information. Moreover, the cuts focusing on lightning and laser events were omitted as well since the CORSIKA shower processing algorithm generates only cosmic-ray events from the input data.

Lists of all applied $X_{\max}$ and SD cuts including their parameters and the number of

events that passed each cut can be found in Appendix B in Tables B.6 - B.10 for each of the three reconstruction methods. The $X_{\mathrm{max}}$ cuts reduced the number of considered events to 2955 HD reconstructed simulations, 3041 simulations reconstructed using the SD geometry and 2208 stereo-reconstructed data. The SD cuts further reduced the HD reconstructed set to 2636 events, and the reconstruction using the SD geometry to 2643 events. The total number of analysed single eye-reconstructed events[1] for the 2636 HD reconstructed showers was 4715. From the 2643 showers reconstructed using the SD geometry there were 4816 eye-reconstructed events, and the 2208 stereo-reconstructed showers comprise of 3810 eye-reconstructed events.

To correct for the simulated energy spectrum with spectral index $\gamma^{\mathrm{MC}} = 1$, each entry in the following profile histograms was weighted by a factor

$$10^{\left(\log_{10}\left(E_{\mathrm{tot}}^{\mathrm{MC}}/1\ \mathrm{eV}\right)-19.5\right)-\left(\gamma^{\mathrm{MC}}-\gamma^{\mathrm{dat}}\right)}, \tag{5.1}$$

where $E_{\mathrm{tot}}^{\mathrm{MC}}$ corresponds to the total simulated shower energy in eV and $\gamma^{\mathrm{dat}}$ corresponds to the spectral index estimated from the Pierre Auger Observatory data [16]. This spectral index is 3.05 for energies from the ankle up to $5 \cdot 10^{19}$ eV and 5.1 for higher energies. Throughout this and the next chapter, the notation $\log_{10}\left(E_{\mathrm{tot}}^{\mathrm{MC}}\right)$ will correspond to $\log_{10}\left(E_{\mathrm{tot}}^{\mathrm{MC}}/1\ \mathrm{eV}\right)$, where the latter was not used for better readability.

## 5.1 Difference in the $X_{\mathrm{max}}$

First, we analysed the difference in the $X_{\mathrm{max}}$ reconstructed using the SD geometry ($X_{\mathrm{max}}^{\mathrm{SDgeom}}$) and $X_{\mathrm{max}}$ reconstructed using the standard hybrid reconstruction method ($X_{\mathrm{max}}^{\mathrm{HD}}$) for only identical eye-reconstructed CORSIKA showers. After the selection of such events using their event IDs and the same FD sites that observed them, we obtained 3672 identical eye-reconstructed events for the HD reconstruction and the reconstruction using the SD geometry. We plotted the mean values of the $X_{\mathrm{max}}$ difference in various $R_{\mathrm{p}}$, $X_{\mathrm{max}}^{\mathrm{MC}}$ and $\log_{10}\left(E_{\mathrm{tot}}^{\mathrm{MC}}\right)$ bins. The respective dependencies are shown on left panels of Figure 5.1. In all three plots, one can immediately notice a constant offset in the reconstructed $X_{\mathrm{max}}$. The $X_{\mathrm{max}}$ differences were fitted by a constant using the $\chi^2$ minimization procedure to help us estimate a factor that would reduce them. We obtained an offset of $(4.8 \pm 0.3)$ g/cm$^2$ for the $R_{\mathrm{p}}$ dependence, $(4.6 \pm 0.3)$ g/cm$^2$ for the $X_{\mathrm{max}}^{\mathrm{MC}}$ dependence and $(5.2 \pm 0.2)$ g/cm$^2$ for the $\log_{10}\left(E_{\mathrm{tot}}^{\mathrm{MC}}\right)$ dependence. From these parameters, we then estimated the correction factor for the reconstruction using the SD geometry as

$$X_{\mathrm{max}}^{\mathrm{SDgeom}} = X_{\mathrm{max}}^{\mathrm{HD}} + 5\ \mathrm{g/cm^2}. \tag{5.2}$$

Analogous approach was applied to the $X_{\mathrm{max}}$ differences between the HD and stereo ($X_{\mathrm{max}}^{\mathrm{Stereo}}$) reconstructions shown on the right panels of Figure 5.1. The number of the same eye-reconstructions in the case of HD and stereo reconstruction methods was 3609. The offsets obtained from the $\chi^2$ minimization procedure were

[1] We refer to individual FD sites as eyes and to the events reconstructed by individual FD sites as eye-reconstructed events.

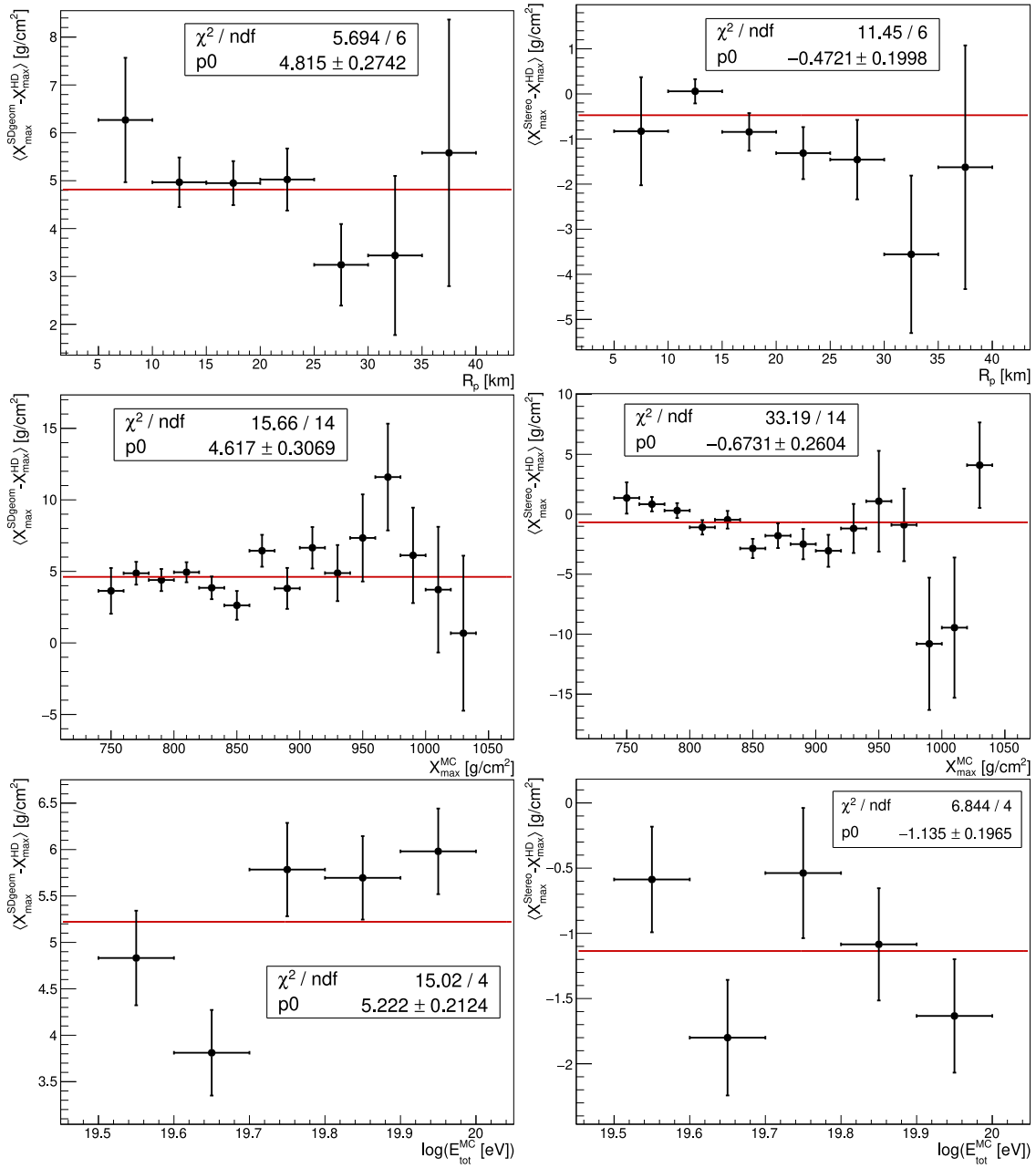


Figure 5.1: Mean value of the difference of the $X_{\max}$ reconstructed with the HD and SD geometry methods (left) and HD and stereo methods (right) in various $R_{\mathrm{p}}$, $X_{\max}^{\mathrm{MC}}$ and $\log_{10}\left(E_{\mathrm{tot}}^{\mathrm{MC}}\right)$ bins for eye-reconstructions of the same CORSIKA showers only.

$(-0.5 \pm 0.2)$ g/cm$^2$ for the $R_{\mathrm{p}}$ dependence, $(-0.7 \pm 0.3)$ g/cm$^2$ for the $X_{\max}^{\mathrm{MC}}$ dependence and $(-1.1 \pm 0.2)$ g/cm$^2$ for the $\log_{10}\left(E_{\mathrm{tot}}^{\mathrm{MC}}\right)$ dependence. From these parameters, we estimated the correction factor for the stereo reconstruction as

$$X_{\max}^{\mathrm{Stereo}} = X_{\max}^{\mathrm{HD}} - 1 \text{ g/cm}^2. \tag{5.3}$$

In Figure 5.2, we show the difference between the reconstructed $(X_{\max}^{\mathrm{rec}})$ and MC simulated $(X_{\max}^{\mathrm{MC}})$ depth of the shower maximum in individual $R_{\mathrm{p}}$, $X_{\max}^{\mathrm{MC}}$ and

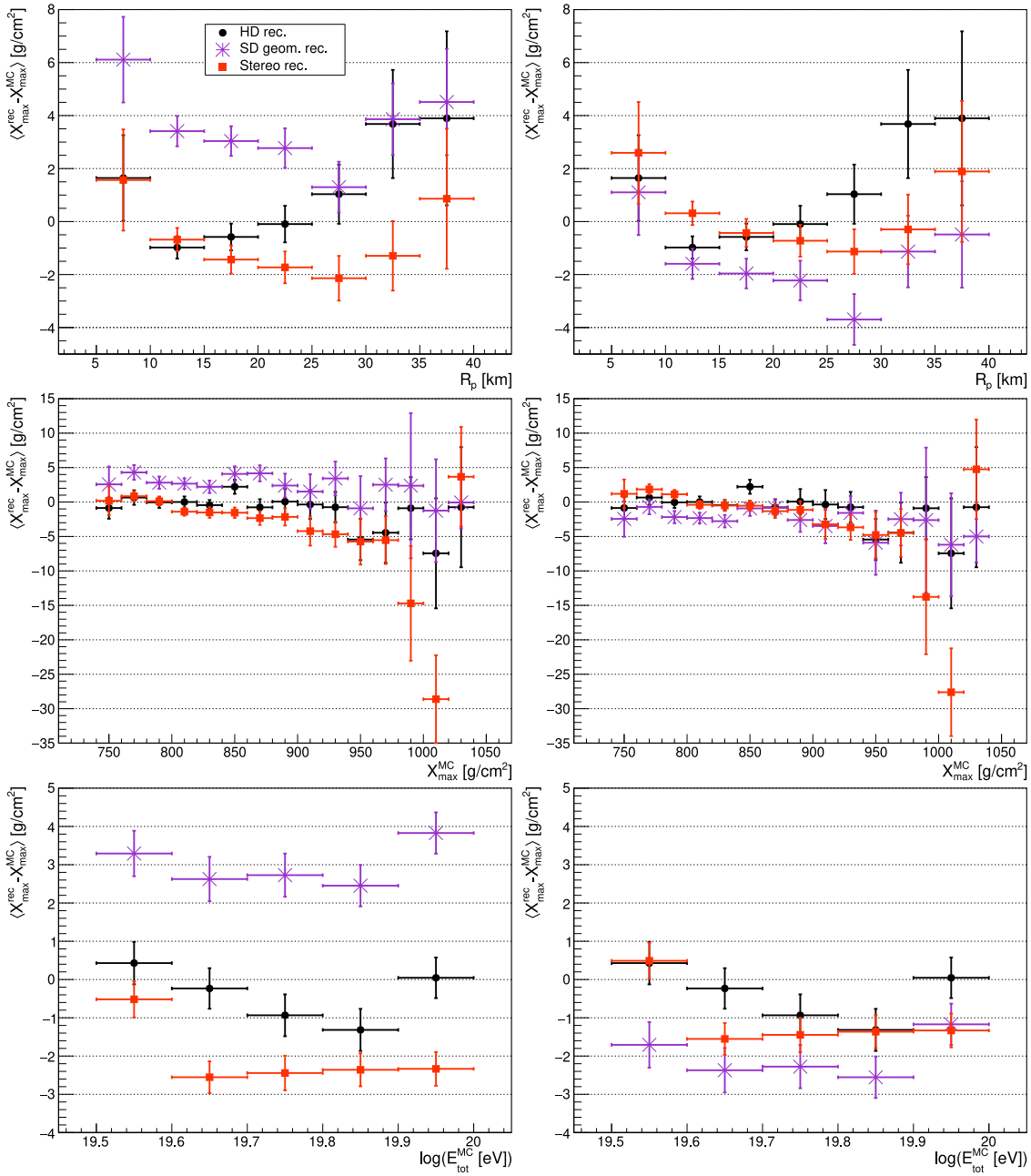


Figure 5.2: Mean value of the $X_{\mathrm{max}}$ bias in different $R_{\mathrm{p}}$, $X_{\mathrm{max}}^{\mathrm{MC}}$ and $\log_{10}\left(E_{\mathrm{tot}}^{\mathrm{MC}}\right)$ bins for the three different reconstruction methods with (right) and without (left) the corrections defined in Eqs. (5.2), (5.3).

$\log_{10}\left(E_{\mathrm{tot}}^{\mathrm{MC}}\right)$ bins for all three methods with (right) and without (left) the previously estimated corrections applied. An overall improvement in the behaviour of the differences in biases for the corrected methods is clearly seen. The most significant change occurs in the dependence on $\log_{10}\left(E_{\mathrm{tot}}^{\mathrm{MC}}\right)$, where the difference between all three methods decreases from more than 4 g/cm$^2$ to about 2 g/cm$^2$. In the dependence on $X_{\mathrm{max}}^{\mathrm{MC}}$, the differences in the $X_{\mathrm{max}}$ bias decrease by using the correction factors for the bins with higher statistic from $\approx 5$ g/cm$^2$ to $\approx 3$ g/cm$^2$.

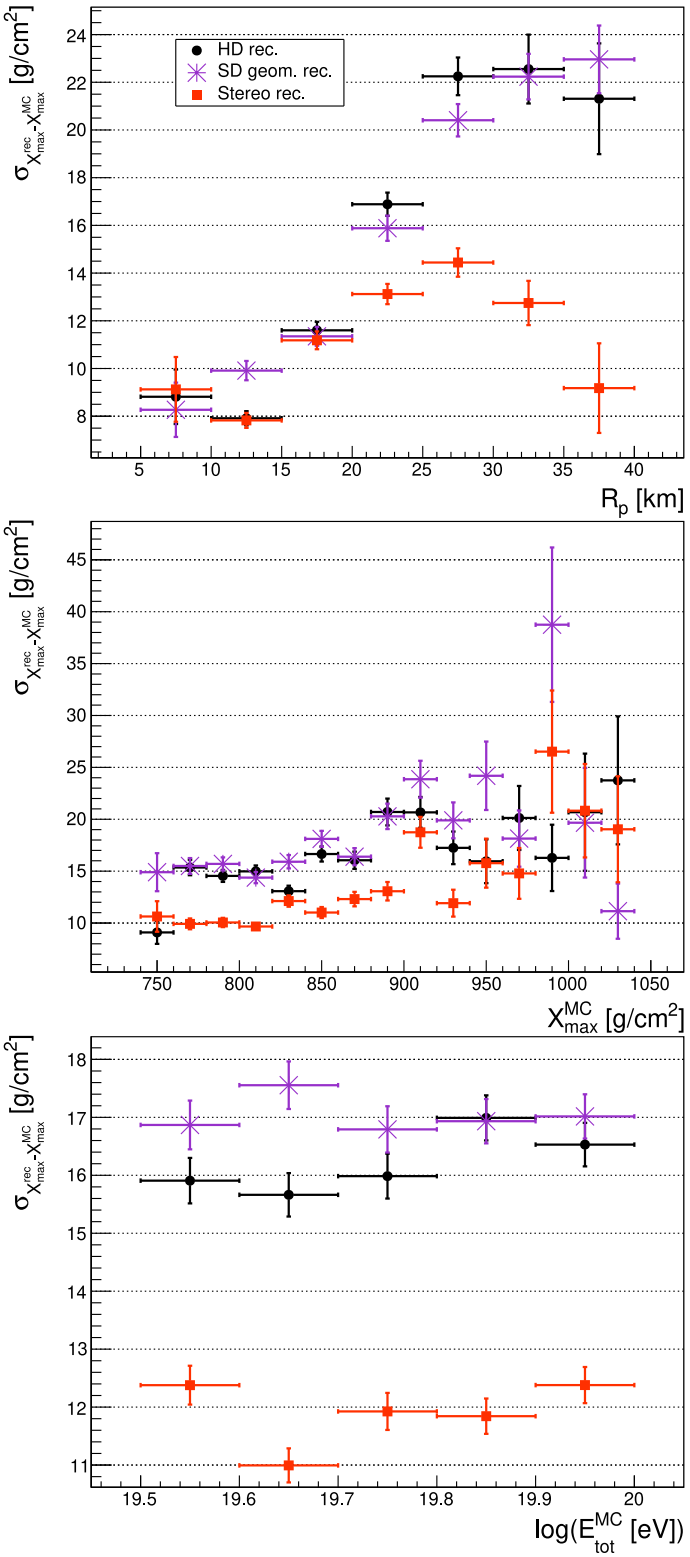


Figure 5.3: Standard deviation of the $X_{\max}$ bias in different $R_{\mathrm{p}}$, $X_{\max}^{\mathrm{MC}}$ and $E_{\mathrm{tot}}^{\mathrm{MC}}$ bins for the three different reconstruction methods.

Finally, Figure 5.3 shows the resolution of the $X_{\max}$ for all three methods. The stereo reconstructed $X_{\max}$ show generally better resolution in comparison with the

other two methods. This improvement results from the shower axis being reconstructed with more precision. The SD geometry $X_{\mathrm{max}}$ resolution is generally worse than the resolution of the other methods, however, the deviations are still within an acceptable region.

## 5.2 Difference in the calorimetric energy

In analogy with the previous section, we plotted the average relative difference in the calorimetric energy $E_{\mathrm{cal}}$ between the HD and SD geometry (HD and stereo) reconstruction methods with respect to $R_{\mathrm{p}}$, $X_{\mathrm{max}}^{\mathrm{MC}}$ and $\log_{10}\left(E_{\mathrm{tot}}^{\mathrm{MC}}\right)$ on the left (right) panels in Figure 5.4 for identical eye-reconstructed CORSIKA showers. $E_{\mathrm{cal}}$ was obtained as the integral of the Gaisser-Hillas function fitted to the longitudinal profile within the Offline software, see Eq. (4.2). We can see that all of the differences are lower than $\approx 5\%$. It implies that the $E_{\mathrm{cal}}$ reconstructed by the two alternative methods does not require any correction factor within our analysis. Using the proton elongation rate $\Lambda^{\mathrm{p}} \approx 58$ g/cm$^2$ [26], we can calculate that such a difference between the energies corresponds to about 1.2 g/cm$^2$ change in the $X_{\mathrm{max}}$. Therefore, it has a negligible effect on the combination of $X_{\mathrm{max}}$ distributions for the three reconstruction methods.

On left panels of Figure 5.5, we show the average relative differences between the three methods in the reconstruction of the calorimetric energy $E_{\mathrm{cal}}^{\mathrm{rec}}$ from the MC values $E_{\mathrm{cal}}^{\mathrm{MC}}$. These differences in bias are compatible with reconstruction differences estimated from Fig. 5.4. The resolutions of $E_{\mathrm{cal}}^{\mathrm{rec}}$ using different reconstruction methods are plotted on the right panels of Fig. 5.5. For the selected stereo showers, the stereo reconstruction provides slightly better resolution than for the HD showers and even a little bit more for reconstruction using the SD geometry. However, these differences could be related to different selections of showers that are differently convenient for the three reconstructions. Again, the effect of these differences for combination of $X_{\mathrm{max}}$ distributions is negligible.

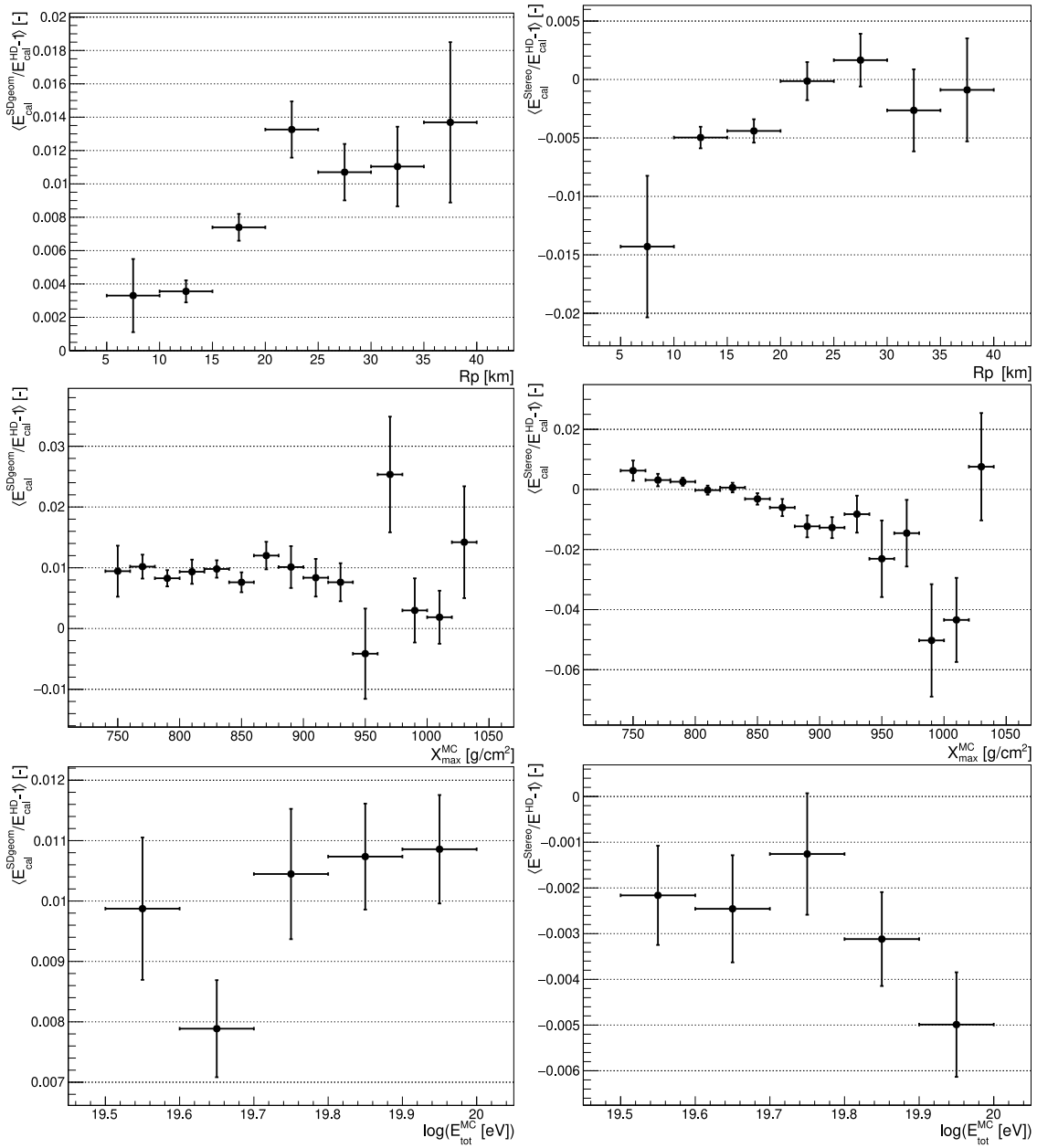


Figure 5.4: Mean relative difference between reconstructed and MC $E_{\mathrm{cal}}$ for comparison of the HD and SD geometry methods (left) and HD and stereo methods (right) in various $R_{\mathrm{p}}$, $X_{\mathrm{max}}^{\mathrm{MC}}$ and $\log_{10}\left(E_{\mathrm{tot}}^{\mathrm{MC}}\right)$ bins for eye-reconstructions of the same CORSIKA showers only.

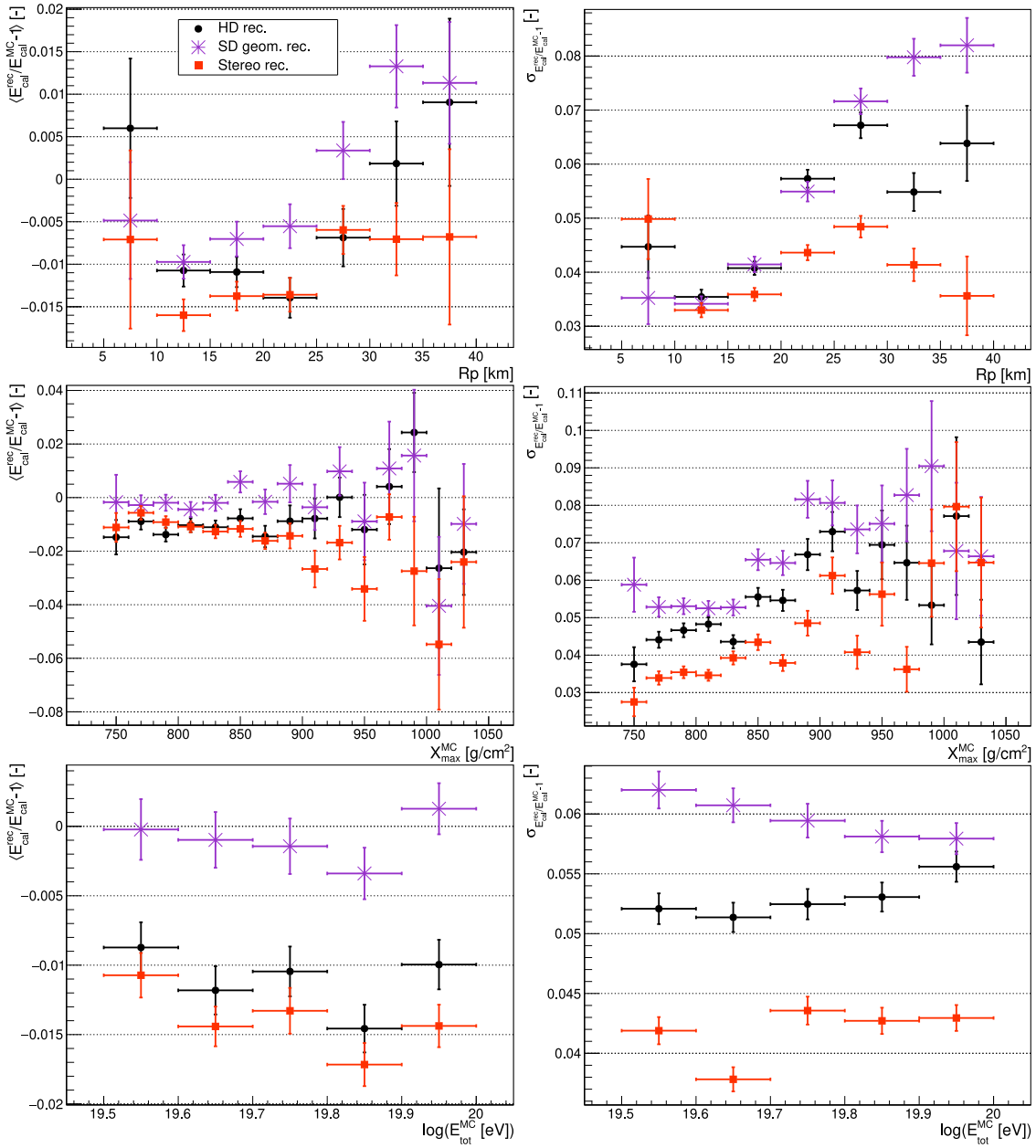


Figure 5.5: Mean value (left) and resolution (right) of the relative reconstructed difference in $E_{\mathrm{cal}}$ from the MC values in various $R_{\mathrm{p}}$, $X_{\mathrm{max}}^{\mathrm{MC}}$ and $\log_{10}\left(E_{\mathrm{tot}}^{\mathrm{MC}}\right)$ bins for the three different reconstruction methods.

## 5.3 Prospects for data analysis

This MC study shows us that simple correction factors applied to the reconstruction methods using the SD geometry and stereo information lower the differences between the $X_{\max}$ biases arising from the three reconstruction methods. Moreover, the resolution of $X_{\max}$ for all three methods is either comparable with acceptable deviations or the alternative method is even better (stereo reconstruction). The calorimetric energy seems to be effected on average within 2% at most with the differences in the resolution within 1.5%. Since the $X_{\max}$ depends logarithmically on energy, we can neglect the differences in the reconstructed calorimetric energy. These results imply that the combination of all three methods, after the simple correction for differences in $X_{\max}$ biases, would provide $X_{\max}$ distributions consistent with the commonly used HD reconstruction in the studied energy range.

To motivate the combination of the three methods even further, we studied on the MC simulations the number of events that passed the selection cuts for reconstruction using the SD geometry, but did not pass it for the HD reconstruction, and the number of events that passed the selection cuts for the reconstruction using stereo geometry only. Here, we considered events with reconstructed FD energy above $10^{19.5}$ eV. This condition lowered the number of HD reconstructed showers from 2636 to 2628 only. The number of new showers that were added by the alternative methods was 218 using the SD geometry and 39 for the stereo reconstruction making the total number of nonidentical showers that passed the selection cuts 2885, increase by $\approx$10%. The number of additional stereo reconstructed showers is limited by the fact that the cores of the CORSIKA showers were simulated only within the SD array. In reality, the stereo reconstruction can potentially increase the analysed data set even more as will be seen in Chapter 6.

Following the estimation of the number of new events added by the alternative reconstruction methods, we compared the $X_{\max}$ distributions resulting from the HD reconstructed events only and from the data set of 2885 unique events that were complemented by the two alternative reconstructions applying the correction factors from Eqs. (5.2),(5.3) using the Kolmogorov-Smirnov test [71]. The distributions were divided into three energy bins and weighted in accordance with Eq. (5.1). The energy bins were set as follows: $10^{19.5} - 10^{19.6}$ eV, $10^{19.6} - 10^{19.7}$ eV and $> 10^{19.7}$ eV. The Kolmogorov-Smirnov test gave compatibility of $\sim 50\%$ for the distributions in the first energy bin, $\sim 21\%$ for the second bin and $\sim 38\%$ for the third bin. In Figure 5.6, we can see the weighted distributions together with their mean values and the resolutions. The similarity of the mean values and the resolutions of both types of distributions in all energy bins give us another reassurance that the combination of the three methods does not introduce unwanted bias.

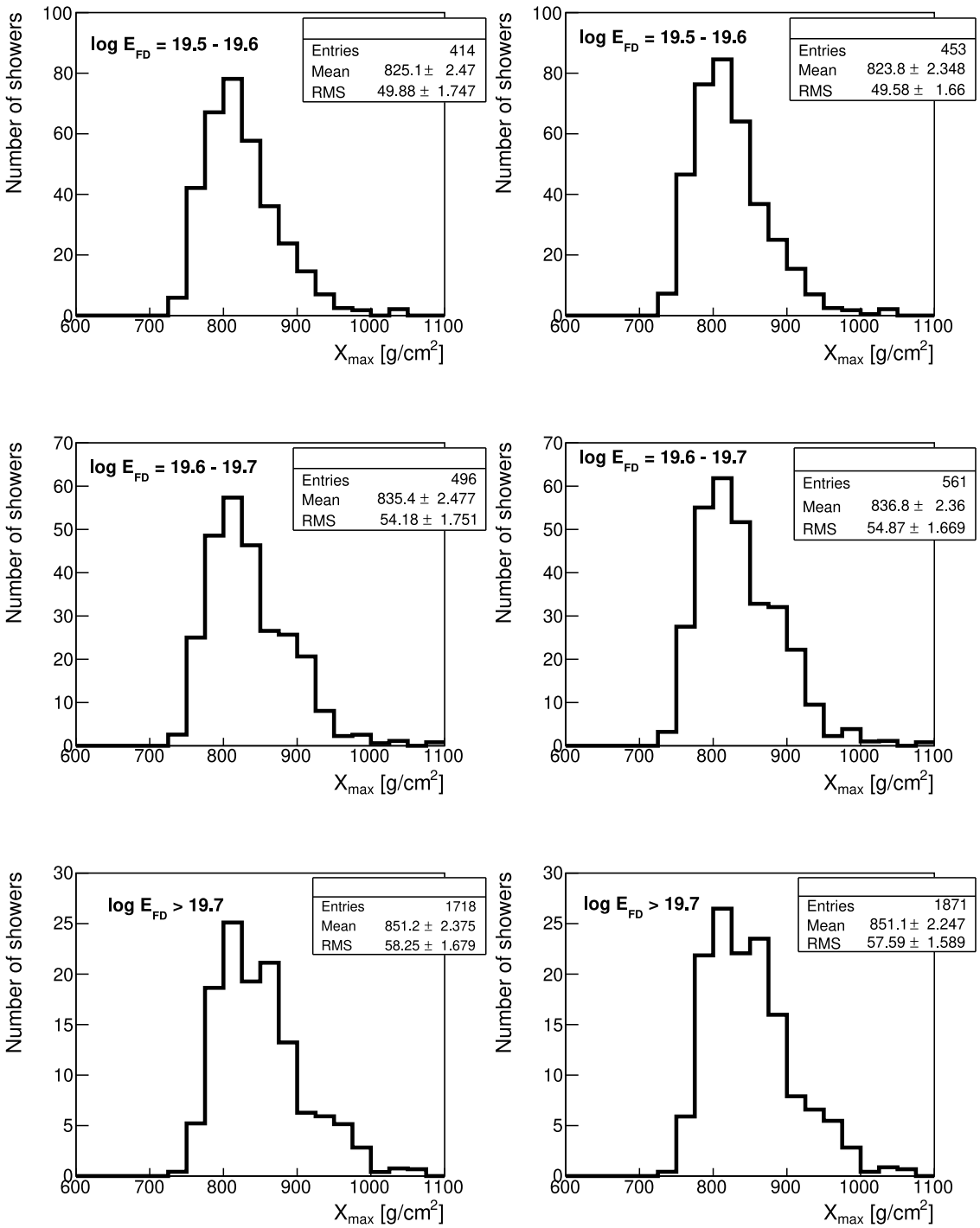


Figure 5.6: Distributions of $X_{\max}$ for HD reconstructed simulated showers only (left) and for the combined set of unique events from all reconstruction methods (right) in three high-energy bins.

# Chapter 6

# Combination of the reconstruction methods using Pierre Auger Observatory data

## 6.1 Selected data

The results presented in this chapter are based on the reconstruction of the Pierre Auger Observatory data taken from 1. 1. 2004 up to the 31. 12. 2018 with energies higher than $10^{19.2}$ eV and zenith angle within 60°. Three methods of the data reconstruction were used - the HD reconstruction, the reconstruction of hybrid events using the SD geometry and the stereo reconstruction. For the HD and stereo reconstruction methods, a set of all Auger detected showers was used, whereas for the reconstruction using the SD geometry, we used only the so-called golden-hybrid data[1]. Unfortunately, we were not able to reconstruct a part of the data using the HD method due to technical difficulties. For this reason, a smaller subset consisting of golden-hybrid events was used in place of the unreconstructed data. The possible consequences of this solution will be discussed later.

The reconstruction and application of the selection cuts was produced through the Offline SVN trunk version 34510. Concerning the cuts applied to the final data, the HD reconstructed showers and the showers reconstructed using the SD geometry were selected through the default set of SD cuts presented in Table A.1 and the default set of $X_{\max}$ cuts from Table A.2 with the *minLgEnergyFD* set to 19.2. For the events reconstructed using the SD geometry, we did not consider the *hybridTankTrigger* and *maxCoreTankDist* cuts as they would not let any event pass because of the different approach to the usage of SD signal for the reconstruction in comparison with the HD reconstruction. For the stereo reconstruction, the same $X_{\max}$ cuts as for the reconstruction using the SD geometry were applied with the additional removal of *minPBrass* and *minPBrassProtonIronDiff* cuts and reparametrization of the *maxZenithFD* cut to 60°. The SD cuts themselves as well as the SD-related cuts

[1]Golden-hybrid data are high-quality events measured by both FD and SD, whereas the standard hybrid events require only one SD station to trigger.

are not applicable to the stereo reconstructed data as these data do not have any reconstructed SD signal. All of the cuts applied to the data reconstructed by the three methods as well as the numbers of events that passed each cut are listed in Tables B.1 - B.5 in Appendix B.

In each figure included in this chapter, we show all of the HD reconstructed events that have passed the selection cuts, the additional events that can be added into the high-quality $X_{\max}$ data set [64] by reconstructing hybrids using the SD geometry, and the additional events that can be added by the stereo reconstruction only. The depths of the shower maximum reconstructed using the SD geometry and with the stereo method were corrected according to Eqs. (5.2),(5.3).

In Figure 6.1, we plot the $X_{\max}$ as a function of $E_{\mathrm{FD}}$ reconstructed from each FD site for the combined set of events from all three reconstruction methods. This scatter plot shows the depths of the shower maximum and the shower energies considered for the following discussion.

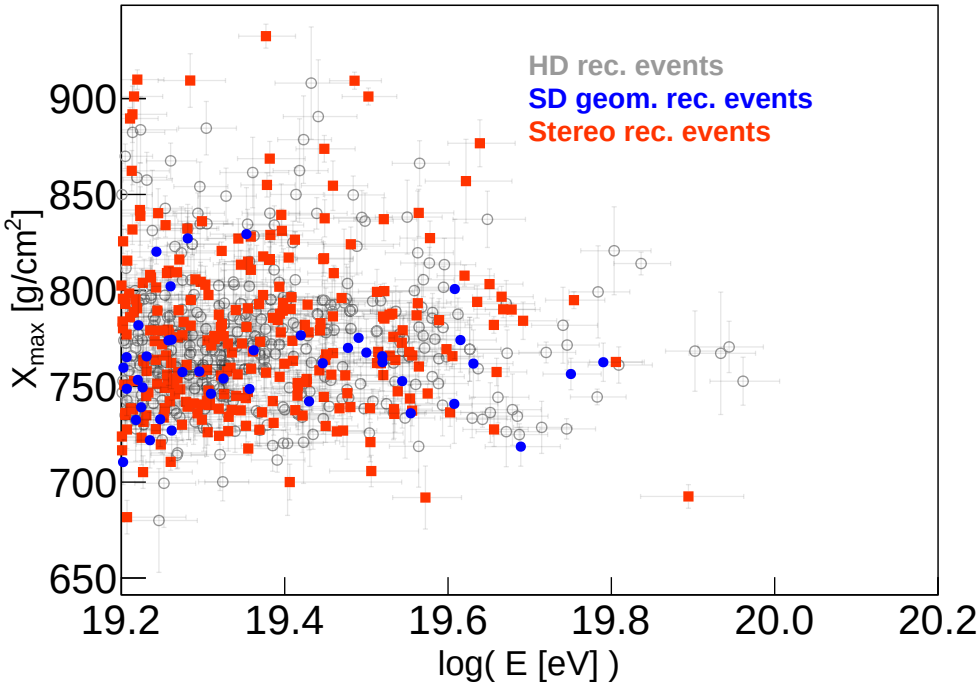


Figure 6.1: Relation between the eye-reconstructed $X_{\max}$ and shower energy for the HD reconstruction (gray), reconstruction using the SD geometry (blue) and stereo reconstruction (orange).

## 6.2 Discussion of the results

In Figure 6.2, we show the number of showers above the FD energy specified on the horizontal axis. For showers observed by more than one FD site, we calculated the average of energies weighted over their reconstructed statistical errors. From these

plots we can read the number of high-quality events above $10^{19.2}$ eV that can be added to the standard $X_{\mathrm{max}}$ analysis of 284 events by using the SD geometry and the stereo reconstruction method without spoiling the information on mass composition of UHECR. The reconstruction using the SD geometry provides 40 unique events to pass the high-quality selection cuts and the stereo reconstruction adds another 221 events. For the higher energies, we can see that the number of stereo reconstructed events starts to decrease in comparison with the HD reconstruction method. This is probably caused by the improved resolution of the shower geometry estimation by the HD method for UHECR showers. On the other hand, the reconstruction using the SD geometry begins to approach the HD reconstruction for highest-energy events. In this case, the behaviour can be explained by an improved reconstruction of the showers that fall farther from the FD sites using the SD geometry.

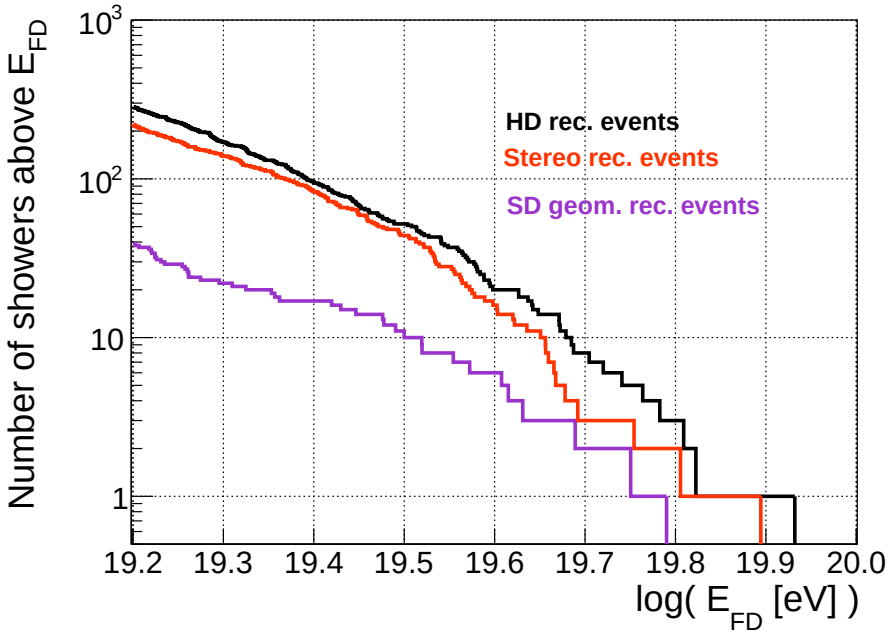


Figure 6.2: The number of detected showers above the logarithm of the reconstructed FD energy for all selected HD reconstructed events (black), events added by the reconstruction using the SD geometry (violet) and events added by the stereo reconstruction (orange).

Concerning the fraction of events added by the stereo reconstruction, we can see that it is much higher than in the case of the simulated showers, see Chapter 5. We assume that this increase is caused by the following reasons:

- The sets of the Pierre Auger Observatory data used for the HD and stereo reconstruction methods were not completely identical.
- The fraction of MC simulated events added by the stereo method is lower due to the predefined positions of the simulated showers directly in the SD array.

- The sets of MC showers used for the stereo reconstruction and reconstruction using the SD geometry were identical, whereas for the Observatory data analysis, the stereo reconstruction was applied on all of the raw data as opposed to the reconstruction using the SD geometry, where only the golden-hybrid events were used.

- Additionally, the MC simulated showers do not take into account misalignment of telescopes or inactive SD stations resulting in a surplus of events reconstructed using the SD geometry that pass the selection cuts.

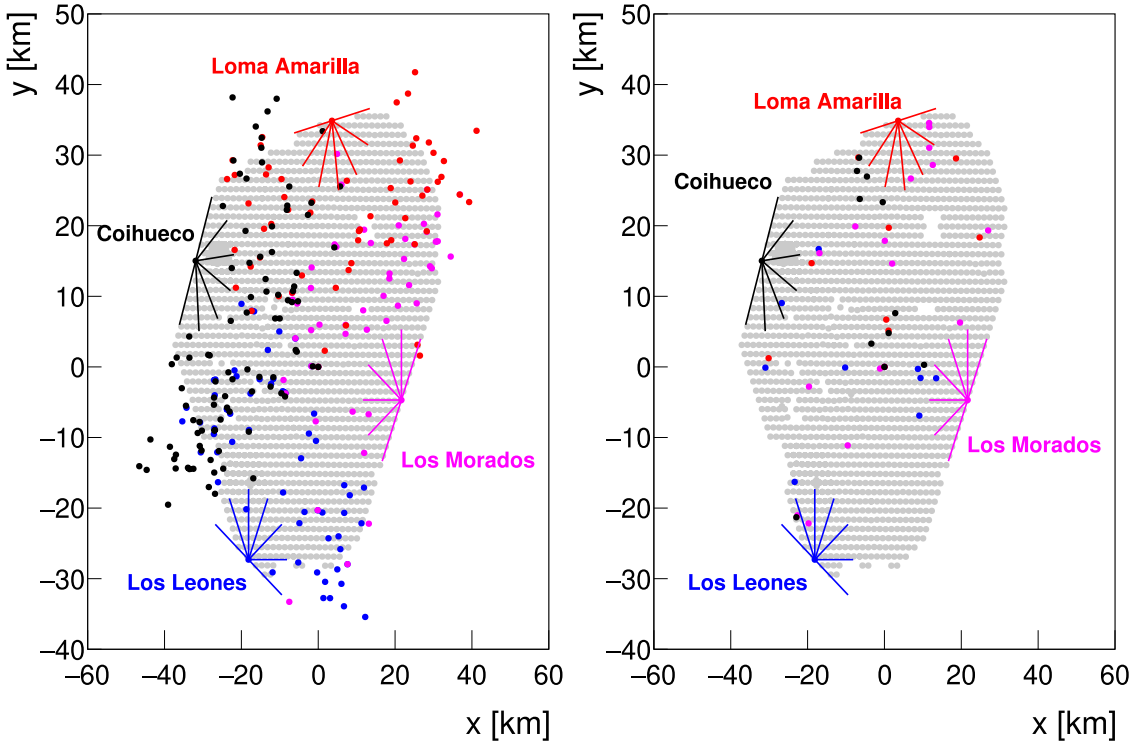


Figure 6.3: Distribution of the shower cores reconstructed by individual FD sites in the Observatory coordinate system. The grey dots correspond to the SD array and the colored lines correspond to the fields of view of respective FD sites. **Left:** Geometry from the stereo reconstruction. **Right:** Geometry from the SD.

Next, we looked at the distributions of the shower cores reconstructed by the two alternative methods. In the left panel of Figure 6.3, we show the distribution of the individual stereo reconstructed FD events in the Observatory coordinate system. By addition of the SD array to the figure, we can see that the stereo reconstructed showers do not fall only directly on the array, but also far outside of it, enlarging the effective area of the Pierre Auger Observatory. The number of the stereo events with zenith angles below 60° and with energies above $10^{19.2}$ eV out of the SD array exceeds 40, giving us the lower bound for the number of high-quality events that can be added to the standard $X_{\mathrm{max}}$ analysis by applying the stereo reconstruction method. The case for the reconstruction using the SD geometry is depicted on the right panel of Figure 6.3. We point out the generally large distances between the reconstructed shower cores and the FD sites that observed them. This result suggests

that the use of SD geometry in hybrid event reconstruction allows more distant events to pass the selection cuts.

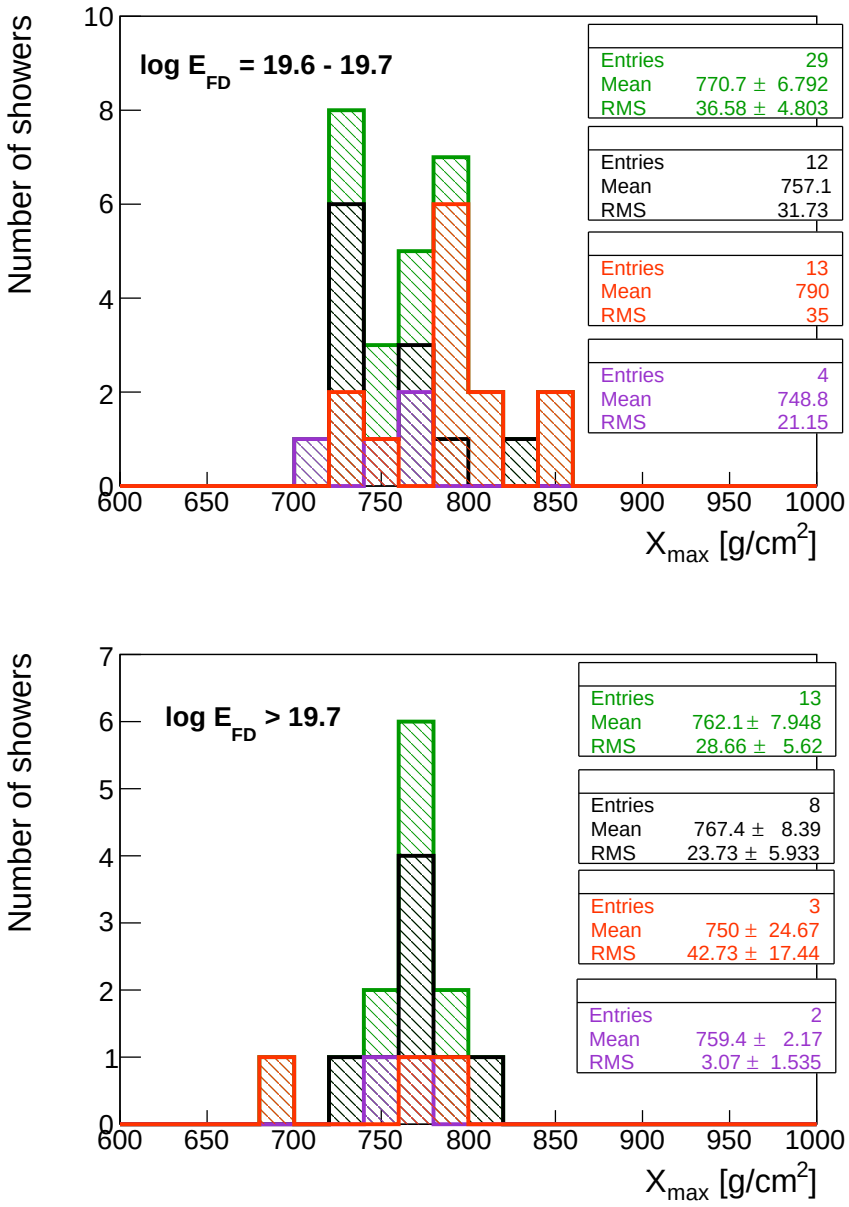


Figure 6.4: $X_{\max}$ distribution of Pierre Auger Observatory data in the two highest-energy bins. Black distribution corresponds to the HD reconstruction, violet to the reconstruction using the SD geometry, orange to the stereo reconstruction and green to the combined data from all three methods.

In Figure 6.4, we show the $X_{\max}$ distributions of the unique events from individual reconstruction methods as well as of all methods combined in the two highest-energy bins. Analogically to the case of the number of events above the FD energy, we considered the weighted average of the energies and $X_{\max}$ for the showers that were observed by more than one FD site. The bins were selected as

$19.6 < \log_{10}(E_{\rm FD}/1\ {\rm eV}) < 19.7$ and $19.7 < \log_{10}(E_{\rm FD}/1\ {\rm eV})$. The bin between 19.6 and 19.7 is not considered in the official $X_{\rm max}$ analysis [72] as the total number of events in that bin does not exceed 40; minimal statistically significant value for a bin agreed within the Collaboration. We plot this energy bin with the ambition to increase the data set above the stated number. We can see in the figure that the number of new events added by the alternative methods is 17, making the total number of events in this energy bin 29. Due to the technical difficulties associated with the HD reconstruction, we can not conclude whether the number of events in this bin would increase with additional HD reconstructed events. Here, however, we limited ourselves by discarding events with zenith angle higher than 60°. For our future analysis of the $X_{\rm max}$ distributions, the showers with higher zenith angles must be taken into account as well to check, whether the number of all possible events included in this energy bin would exceed 40. Concerning the bin with energies greater than $10^{19.7}$ eV, the number of events with zenith angles lower than 60° added to the 8 HD reconstructed events by the alternative methods is 5.

# Conclusions

Three reconstruction methods of the Pierre Auger Observatory data were applied in this work. The standard hybrid reconstruction was complemented by two alternative reconstructions of FD data: using the SD geometry, and geometry obtained by combining multiple FD telescopes.

We have studied the differences between the three reconstruction methods in the depth of shower maximum ($X_{\mathrm{max}}$) and calorimetric energy ($E_{\mathrm{cal}}$) for simulated showers of energies $10^{19.5-20}$ eV. We have proposed simple correction factors in $X_{\mathrm{max}}$ for the two alternative methods minimizing the differences in biases between the three reconstruction methods within 5 g/cm$^2$. The average relative differences in $E_{\mathrm{cal}}$ were found within 2%, which is negligible compared to the total systematic uncertainties of the energy scale (14%), with an effect on $X_{\mathrm{max}}$ within 1.2 g/cm$^2$. We have also studied the resolution of both $X_{\mathrm{max}}$ and $E_{\mathrm{cal}}$ indicating very similar values between the three reconstruction methods. This MC analysis demonstrates that the potential combination of the events reconstructed by the three methods would be consistent with the $X_{\mathrm{max}}$ distributions of the standard hybrid reconstruction. The estimated increase of new events with reliable $X_{\mathrm{max}}$ information is about 10% for energies above $10^{19.5}$ eV within 60° of zenith angle.

Following the analysis of the biases between the three different reconstruction methods and estimation of the simple correction factors, we have examined the combination of the different methods on the Pierre Auger Observatory data. The number of events reconstructed using the HD method that satisfied the high-quality selection cuts above the energy $10^{19.2}$ eV and within the zenith angle 60° was 284. We have shown that the number of showers added by the two alternative methods exceeds 250, being inconsistent with the conclusion from the analysis conducted on the simulated data. We have attributed this behaviour to four factors, namely that we were not able to apply the HD reconstruction to the whole data set to which the stereo method was applied, the stereo reconstruction applied to the simulated showers could not add any events lying outside of the SD array, the input data for the stereo and SD geometry reconstruction were identical for the MC showers, which was not the case for the real Observatory data, where the number of raw events reconstructed using the SD geometry was lower than for the stereo reconstruction, and, finally, the MC simulations used did not take into account misalignment of telescopes or inactive SD stations.

For further analysis we will study the biases between the different methods for simulated showers initiated by heavier nuclei. We will also include simulated showers with cores outside of the SD array. We will enlarge the zenith angle range in case of hybrid and stereo reconstructions up to 80°. For the study of the impact of

the combination of the three methods on the Observatory data we will try to finish the HD reconstruction of all the data and determine the total number of new events that pass the selection cuts by using the two alternative methods. A more thorough analysis of the stereo reconstructed events will be conducted as well to conclude whether some additional cuts need to be applied to ensure the desired quality of the selected events.

# Bibliography


[1] C. A. Coulomb. *Premier-[troisième] mémoire sur l'electricité et le magnétisme.* Nineteenth Century Collections Online (NCCO): Science, Technology, and Medicine: 1780-1925. Académie Royale des sciences, 1785.

[2] C. T. R. Wilson. On the ionisation of atmospheric air. *Proceedings of the Royal Society of London*, 68:151 – 161, 1901.

[3] A. De Angelis and M. J. M: Pimenta. *Introduction to Particle and Astroparticle Physics: Questions to the Universe.* Undergraduate lecture notes in physics. Springer, Milan, Jul 2015.

[4] V. F. Hess. Über Beobachtungen der durchdringenden Strahlung bei sieben Freiballonfahrten. *Phys. Zeit.*, 13:1084–1091, 1912.

[5] V. F. Hess. Über den Ursprung der durchdringenden Strahlung. *Phys. Zeit.*, 14:610–617, 1913.

[6] J. Clay and H. P. Berlage. Variation der Ultrastrahlung mit der geographischen Breite und dem Erdmagnetismus. *Die Naturwissenschaften*, 20:687–688, 1932.

[7] L. Alvarez and A. H. Compton. A Positively Charged Component of Cosmic Rays. *Phys. Rev.*, 43:835–836, May 1933.

[8] T. H. Johnson. The Azimuthal Asymmetry of the Cosmic Radiation. *Phys. Rev.*, 43:834–835, May 1933.

[9] P. Auger, P. Ehrenfest, R. Maze, J. Daudin, and Robley A. Fréon. Extensive cosmic-ray showers. *Rev. Mod. Phys.*, 11:288–291, Jul 1939.

[10] H. Yukawa. On the Interaction of Elementary Particles I. *Proc. Phys. Math. Soc. Jap.*, 17:48–57, 1935.

[11] C. D. Anderson and S. H. Neddermeyer. Cloud Chamber Observations of Cosmic Rays at 4300 Meters Elevation and Near Sea-Level. *Phys. Rev.*, 50:263–271, Aug 1936.

[12] C. M. G. Lattes, G. P. S. Occhialini, and C. F. Powell. Observations on the Tracks of Slow Mesons in Photographic Emulsions. 1. *Nature*, 160:453–456, 1947.

[13] A. Aab et al. Observation of a large-scale anisotropy in the arrival directions of cosmic rays above $8 \times 10^{18}$ eV. *Science*, 357(6357):1266–1270, Sep 2017.

[14] A. D. Erlykin and A. W. Wolfendale. The knee in the cosmic ray energy spectrum, 2009.

[15] J. R. Hörandel. Cosmic Rays From The Knee To The Second Knee: $10^{14}$ To $10^{18}$ eV. *Modern Physics Letters A*, 22(21):1533–1551, Jul 2007.

[16] A. Aab et al. Measurement of the cosmic-ray energy spectrum above $2.5{\times}10^{18}$ eV using the Pierre Auger Observatory. *Phys. Rev. D*, 102(6):062005, 2020.

[17] K. Greisen. End to the Cosmic-Ray Spectrum? *Phys. Rev. Lett.*, 16:748–750, Apr 1966.

[18] G. T. Zatsepin and V. A. Kuzmin. Upper limit of the spectrum of cosmic rays. *JETP Lett.*, 4:78–80, 1966.

[19] D. H. Perkins. *Particle Astrophysics, Second Edition*. Oxford Master Series in Physics. OUP Oxford, 2009.

[20] S.P. Swordy. The Energy Spectra and Anisotropies of Cosmic Rays. *Space Science Reviews*, 99:85–94, Oct 2001.

[21] E. Fermi. On the Origin of the Cosmic Radiation. *Phys. Rev.*, 75:1169–1174, 1949.

[22] A. López-Oramas. *Multi-year Campaign of the Gamma-Ray Binary LS I +61∘ 303 and Search for VHE Emission from Gamma-Ray Binary Candidates with the MAGIC Telescopes*. PhD thesis, Apr 2015.

[23] W. Heitler. *The Quantum Theory of Radiation*. Oxford University Press, London, third edition, 1954.

[24] S. Mollerach and E. Roulet. Progress in high-energy cosmic ray physics. *Progress in Particle and Nuclear Physics*, 98:85–118, Jan 2018.

[25] P.A. Zyla et al. Review of Particle Physics. *PTEP*, 2020(8):083C01, 2020. and 2021 update.

[26] J. Matthews. A Heitler model of extensive air showers. *Astroparticle Physics*, 22(5):387 – 397, 2005.

[27] J. Alvarez-Muñiz, R. Engel, T. K. Gaisser, J. A. Ortiz, and T. Stanev. Hybrid simulations of extensive air showers. *Phys. Rev. D*, 66(3):033011, Aug 2002.

[28] Particle Data Group. Review of Particle Properties. *Phys. Rev. D*, 66:258, Jul 2002.

[29] J. Engel, T. K. Gaisser, P. Lipari, and T. Stanev. Nucleus-nucleus collisions and interpretation of cosmic-ray cascades. *Phys. Rev. D*, 46:5013–5025, Dec 1992.

[30] J. W. Fowler, L. F. Fortson, C. C. H. Jui, D. B. Kieda, R. A. Ong, C. L. Pryke, and P. Sommers. A measurement of the cosmic ray spectrum and composition at the knee. *Astroparticle Physics*, 15(1):49–64, Mar 2001.

[31] T. Antoni et al. The Cosmic ray experiment KASCADE. *Nucl. Instrum. Meth. A*, 513:490–510, 2003.

[32] T. Huege et al. The LOPES experiment—recent results, status and perspectives. *Nuclear Instruments and Methods in Physics Research Section A: Accelerators, Spectrometers, Detectors and Associated Equipment*, 662:S72–S79, Jan 2012.

[33] D. Heck, J. Knapp, J. N. Capdevielle, G. Schatz, and T. Thouw. CORSIKA: A Monte Carlo code to simulate extensive air showers. Feb 1998.

[34] D. J. Bird et al. Detection of a cosmic ray with measured energy well beyond the expected spectral cutoff due to cosmic microwave radiation. *The Astrophysical Journal*, 441:144, Mar 1995.

[35] P. Sokolsky. Final Results from the High Resolution Fly's Eye (HiRes) Experiment. *Nuclear Physics B - Proceedings Supplements*, 212–213:74–78, Mar 2011.

[36] A. Aab et al. The Pierre Auger Cosmic Ray Observatory. *Nuclear Instruments and Methods in Physics Research Section A: Accelerators, Spectrometers, Detectors and Associated Equipment*, 798, Feb 2015.

[37] A. Aab et al. Spectral Calibration of the Fluorescence Telescopes of the Pierre Auger Observatory. *Astroparticle Physics*, 95, Sep 2017.

[38] A. Filipcic, D. Veberic, M. Zavrtanik, and D. Zavrtanik. Pierre Auger Atmospheric-Monitoring LIDAR System. Jan 2001.

[39] A. Castellina. AugerPrime: the Pierre Auger Observatory Upgrade. *EPJ Web of Conferences*, 210:06002, 2019.

[40] S. Argirò, S.L.C. Barroso, J. Gonzalez, L. Nellen, T. Paul, T.A. Porter, L. Prado Jr., M. Roth, R. Ulrich, and D. Veberič. The Offline Software Framework of the Pierre Auger Observatory. *Nuclear Instruments and Methods in Physics Research Section A: Accelerators, Spectrometers, Detectors and Associated Equipment*, 580(3):1485–1496, Oct 2007.

[41] J. Vicha and J. Chudoba. Data Processing at the Pierre Auger Observatory. *Journal of Physics: Conference Series*, 608:012077, May 2015.

[42] T. Bergmann, R. Engel, D. Heck, N. Kalmykov, S. Ostapchenko, T. Pierog, T. Thouw, and K. Werner. One-dimensional hybrid approach to extensive air shower simulation. *Astroparticle Physics*, 26(6):420–432, Jan 2007.

[43] A. M. Hillas. Shower simulation: lessons from MOCCA. *Nuclear Physics B - Proceedings Supplements*, 52(3):29–42, 1997.

[44] S. Ostapchenko. Monte Carlo treatment of hadronic interactions in enhanced Pomeron scheme: QGSJET-II model. *Physical Review D*, 83(1), Jan 2011.

[45] S. Ostapchenko. Hadronic Interactions in QGSJET-II: Physics and Results. Aug 2005.

[46] R. S. Fletcher, T. K. Gaisser, P. Lipari, and T. Stanev. Sibyll: An event generator for simulation of high energy cosmic ray cascades. *Phys. Rev. D*, 50:5710–5731, Nov 1994.

[47] K. Werner, F.-M. Liu, and T. Pierog. Parton ladder splitting and the rapidity dependence of transverse momentum spectra in deuteron-gold collisions at the BNL Relativistic Heavy Ion collider. *Physical Review C*, 74(4), Oct 2006.

[48] V. N. Gribov. A Reggeon Diagram Technique. *Zh. Eksp. Teor. Fiz.*, 53:654–672, 1967.

[49] F. Riehn, R. Engel, A. Fedynitch, T. K. Gaisser, and T. Stanev. Hadronic interaction model Sibyll 2.3d and extensive air showers. *Physical Review D*, 102(6), Sep 2020.

[50] N. N. Kalmykov, S. S. Ostapchenko, and A. I. Pavlov. Quark-Gluon String Model and EAS Simulation Problems at Ultra-High Energies. *Nucl. Phys. B Proc. Suppl.*, 52:17–28, 1997.

[51] A. B. Kaidalov and K. A. Ter-Martirosian. Multiple Production of Hadrons at High-Energies in the Model of Quark-Gluon Strings. *Sov. J. Nucl. Phys.*, 39:979, 1984.

[52] T. K. Gaisser and F. Halzen. Soft Hard Scattering in the TeV Range. *Phys. Rev. Lett.*, 54:1754, 1985.

[53] G. Pancheri and Y. N. Srivastava. Jets in Minimum Bias Physics. *Conf. Proc. C*, 850313:28, 1985.

[54] G. Pancheri and Y. N. Srivastava. Low-pt jets and the rise with energy of the inelastic cross section. *Physics Letters B*, 182(2):199–207, 1986.

[55] L. Durand and P. Hong. QCD and Rising Total Cross-Sections. *Phys. Rev. Lett.*, 58:303–306, 1987.

[56] R. J. Glauber and G. Matthiae. High-energy scattering of protons by nuclei. *Nucl. Phys. B*, 21:135–157, 1970.

[57] T. Pierog and K. Werner. EPOS Model and Ultra High Energy Cosmic Rays. *Nuclear Physics B - Proceedings Supplements*, 196:102–105, Dec 2009.

[58] T. Pierog, Iu. Karpenko, J. M. Katzy, E. Yatsenko, and K. Werner. EPOS LHC: Test of collective hadronization with data measured at the CERN Large Hadron Collider. *Physical Review C*, 92(3), Sep 2015.

[59] T. Pierog. LHC data and extensive air showers. *EPJ Web Conf.*, 52:03001, 2013.

[60] H. J. Drescher, M. Hladik, S. Ostapchenko, T. Pierog, and K. Werner. Parton-based Gribov–Regge theory. *Physics Reports*, 350(2-4):93–289, Sep 2001.

[61] W. R. Nelson, H. Hirayama, and D. W. O. Rogers. The Egs4 Code System. Dec 1985.

[62] J. N. Capdevielle and J. Gawin. The radial electron distribution in extensive air showers. *Journal of Physics G: Nuclear Physics*, 8(9):1317–1335, Sep 1982.

[63] J. N. Capdevielle. Local Age Parameter and Size Estimation in EAS. In *22nd International Cosmic Ray Conference*, volume 4, pages 405–408, Aug 1991.

[64] A. Aab et al. Depth of Maximum of Air-Shower Profiles at the Pierre Auger Observatory: Measurements at Energies above $10^{17.8}$ eV. *Phys. Rev. D*, 90(12), Dec 2014.

[65] J. Nou, R. Chauvin, S. Thil, and S. Grieu. A new approach to the real-time assessment of the clear-sky direct normal irradiance. *Applied Mathematical Modelling*, 40, Mar 2016.

[66] T. Gaisser and A. Hillas. Reliability of the method of constant intensity cuts for reconstructing the average development of vertical showers. 1977.

[67] D. Kuempel, K. Kampert, and M. Risse. Geometry reconstruction of fluorescence detectors revisited. *Astropart. Phys.*, 30(4):167–174, Nov 2008.

[68] C. Bonifazi. The angular resolution of the Pierre Auger Observatory. *Nuclear Physics B - Proceedings Supplements*, 190:20–25, May 2009.

[69] A. Aab et al. Data-driven estimation of the invisible energy of cosmic ray showers with the Pierre Auger Observatory. *Phys. Rev. D*, 100(8), Oct 2019.

[70] S. Agostinelli et al. GEANT4–a simulation toolkit. *Nucl. Instrum. Meth. A*, 506:250–303, 2003.

[71] N. V. Smirnov. Estimate of deviation between empirical distribution functions in two independent samples. *Bull Moscow University*, 3616(2), 1939.

[72] A. Yushkov. Mass Composition of Cosmic Rays with Energies above $10^{17.2}$ eV from the Hybrid Data of the Pierre Auger Observatory. *PoS*, ICRC2019:482, 2019.

# Appendix A

# Offline supplement

## A.1 Reconstruction setup

As it was already mentioned in the Chapter 2.2, the reconstruction of events detected at the Pierre Auger Observatory is performed within the Auger Offline framework [40]. By default, this framework offers a number of different reconstruction methods, but users are free to specify the processing modules that they want to use in the *ModuleSequence* file. Moreover, users are also able to write their own modules that can be used instead of the default ones, or rewrite parameters in existing modules through the configuration files. The reconstruction itself is then executed through the command `userAugerOffline -b bootstrap.xml`. The XML file called *bootstrap* links the framework to all relevant external configuration files. Through the *bootstrap* file, users have the option to overwrite default parameters of specified modules.

Each reconstruction begins with the *EventFileReaderOG* module connecting the reconstruction algorithm with raw or simulated data. In the configuration file for *EventFileReaderOG*, users need to specify the file type of the input data (e.g. type IoAuger for raw Observatory data or type CORSIKA for CORSIKA simulated data) and the paths to the input data. The paths can be written either explicitly in the configuration file itself or in a text file that is subsequently read by the configuration file. For reconstruction of a higher number of data files, the input through the text file is more practical. The *ModuleSequence* can then be set to loop the modules over all of the input files.

At the end of the reconstruction module sequence, there should always be the *RecDataWriterNG* module to save the reconstruction output in the ADST file. Within the configuration file of this module, users can specify which information they want to be stored. The *RecDataWriterNG* does not store the reconstructed data only, but it also connects the events to their respective atmospheric conditions and other data from the Observatory databases.

## A.2 Selection cuts

Apart from the instruments used for e.g. reconstruction or simulation of cosmic-ray showers, Auger Offline also includes selection cuts that can be applied on the ADST files through a cutting algorithm. By applying these cuts, users can discard those reconstructed events that do not satisfy the requirements for the desired data analysis. Generally, the cuts included in the Auger Offline can be divided into SD, FD, RD (radio detector) and simulation cuts. From all these cuts, the Pierre Auger Collaboration came up with several sets intended for specific types of data analysis. These collections of cuts are written in a text file format and are connected with the cutting algorithm through individual configuration files. Inside each text file, users can change the parameters of individual cuts or add and remove cuts based on their needs. The two most fundamental sets for the purposes of this work are the standard cuts for the $X_{\mathrm{max}}$ analysis and the SD cuts for vertical showers. The $X_{\mathrm{max}}$ cuts are applied separately to the individual FD sites. The set of SD cuts for vertical showers with their default parameters is shown in Table A.1 and the $X_{\mathrm{max}}$ analysis cuts with their default parameters are in Table A.2.

As can be seen in both Table A.1 and Table A.2, some of the cuts do not have any parameter. These cuts are of Boolean data type and their usage is analogous to the usage of bool in C++ codes. This means that if there is an exclamation mark before such a cut, the cutting algorithm selects events that do not satisfy the specified condition. A perfect example of this are the first two cuts from the standard $X_{\mathrm{max}}$ subset (Table A.2). The *isCLF* and *isXLF* cuts examine if the detected event was caused by the two Observatory laser facilities, the CLF and the XLF.

The other Boolean cuts in the standard $X_{\mathrm{max}}$ subset are *badFDPeriodRejection* rejecting events from the FD periods with GPS glitches and bad calibration constants, *good10MHzCorrection* selecting only events with good correction of the 10 MHz oscillator, *hasMieDatabase* rejecting events without atmospheric monitoring and *skipSaturated* discarding events with at least one saturated telescope pixel. The Boolean cuts in the SD vertical subset (Table A.1) are *lightning* rejecting events triggered by a lightning, and *badPeriodsRejectionFromFile* removing SD events registered within periods specified in an external text file. The remaining SD vertical cuts are used for rejection of events without the lateral distribution function (LDF) fit (*minRecLevel* set to 3), removal of inclined events (*maxZenithSD* set to 60), and events without the SD trigger on shower physics (*T4Trigger* set to 2), rejection of events without the 6T5 trigger[1] (*T5Trigger* set to 2) and, finally, *minLgEnergySD* for rejection of events with lower reconstructed SD energy than $10^{17.5}$ eV.

One of the most crucial cuts for the selection of high-quality $X_{\mathrm{max}}$ data is the *FidFOVICRC13* cut ensuring that the telescope field of view (FOV) is large enough to cover all plausible $X_{\mathrm{max}}$ values with high precision. The two parameters of this cut represent the maximum expected uncertainty in the $X_{\mathrm{max}}$ reconstruction and the minimum viewing angle of the telescope[2]. The values of 40 g/cm$^2$ and 20° have been derived for the International Cosmic Ray Conference (ICRC) in 2013 and are

[1] 6T5 trigger accepts only events containing a SD station with the highest signal that is surrounded by 6 other operating SD stations [36].

[2] Telescope viewing angle is defined in Chapter 4.2.

being used onward. Other $X_{\max}$ analysis cuts to be described are the *eyeCut* used to either accept (cut set to 1) or reject (cut set to 0) events detected by specific FD sites, *badPixels* rejecting events with bad telescope pixels, *maxVAOD* accepting events with measured vertical aerosol optical depth (VAOD) integrated from the ground to 3 km less than 0.1, *maxCoreTankDist* selecting events with smaller distance than 1500 m between the FD reconstructed shower core and the closest triggered SD station, *maxZenithFD* discarding events with the FD reconstructed zenith angle greater than 90°, *minLgEnergyFD*[3] accepting events with higher FD reconstructed shower energy than what is specified, *maxDepthHole* removing events with an undetected part of the shower profile larger than 10% of the whole observed profile and, finally, *depthTrackLength* accepting only events with observed shower track length larger than 200 g/cm2.

| Cut | Default parameters |
|---|---|
| !lightning | - |
| minRecLevel | 3 |
| max ZenithSD | 60 |
| T4Trigger | 2 |
| T5Trigger | 2 |
| minLgEnergySD | 17.5 |
| badPeriodsRejectionFromFile | - |

Table A.1: The default subset of SD quality cuts for vertical showers.

[3]Cut *minLgEnergyFD* is used twice in the default subset for the $X_{\max}$ analysis. The first usage is to check, if the event has successfully reconstructed FD energy, and the second usage to specify the minimum required energy.

| Cut | Default parameters |
|---|---|
| !isCLF | - |
| !isXLF | - |
| keepHECOorCoihuecoHEAT | 18.1 {nMinusOne: 21 -10.5 10.5} |
| eyeCut | 1111 |
| badFDPeriodRejection | - |
| minMeanPixelRMSMergedEyes | {params: 17 6 110000 nMinusOne: 100 0 100} |
| minMeanPixelRMSSimpleEye | {params: 17 11111 nMinusOne: 100 0 100} |
| !badPixels | 1 |
| good10MHzCorrection | - |
| hasMieDatabase | - |
| maxVAOD | 0.1 |
| cloudCutXmaxPRD14 | {params: 1 nMinusOne: 21 -10.5 10.5} |
| hybridTankTrigger | 2 |
| maxCoreTankDist | 1500 |
| maxZenithFD | 90 |
| minLgEnergyFD | 1e-20 |
| skipSaturated | - |
| minPBrass | 0.9 |
| maxPBrassProtonIronDiff | 0.05 |
| minLgEnergyFD | 17.8 |
| FidFOVICRC13 | 40 20 |
| xMaxObsInExpectedFOV | {params: 40 20} |
| maxDepthHole | 20. |
| profileChi2Sigma | {params: 3 -1.1 nMinusOne: 400 -20 20} |
| depthTrackLength | 200 |

Table A.2: The default subset of standard $X_{\max}$ analysis cuts.

# Appendix B

# Event selection tables

| Cut | Parameter | Events passed |
|---|---|---|
| nTot | - | $9.27 \cdot 10^6$ |
| !isCLF | - | $9.02 \cdot 10^6$ |
| !isXLF | - | 8967790 |
| keepHECOorCoihuecoHEAT | 18.1 | 6841112 |
| eyeCut | 1111 | 5166887 |
| badFDPeriodRejection | - | 4540367 |
| minMeanPixelRMSMergedEyes | (17, 6, 110000) | 4540367 |
| minMeanPixelRMSSimpleEye | (17, 11111) | 2850533 |
| !badPixels | 1 | 2593783 |
| good10MHzCorrection | - | 2571066 |
| hasMieDatabase | - | 2275392 |
| maxVAOD | 0.1 | 2078094 |
| cloudCutXmaxPRD14 | 1 | 1639238 |
| hybridTankTrigger | 2 | 626232 |
| maxCoreTankDist | 1500 | 624156 |
| maxZenithFD | 90 | 622912 |
| minLgEnergyFD | 1e-20 | 568474 |
| skipSaturated | - | 567114 |
| minPBrass | 0.9 | 495422 |
| maxPBrassProtonIronDiff | 0.05 | 472442 |
| minLgEnergyFD | 19.2 | 1830 |
| FidFOVICRC13 | (40, 20) | 695 |
| xMaxObsInExpectedFOV | (40, 20) | 683 |
| maxDepthHole | 20 | 675 |
| profileChi2Sigma | (3, -1.1) | 640 |
| depthTrackLength | 200 | 640 |

Table B.1: Number of HD reconstructed Pierre Auger Observatory events that passed individual $X_{\max}$ cuts; nTot corresponds to the total number of eye-reconstructed events processed.

| Cut | Parameter | Events passed |
|---|---|---|
| nTot | - | 500 |
| !lightning | - | 500 |
| minRecLevel | 3 | 491 |
| maxZenithSD | 60 | 410 |
| T4Trigger | 2 | 410 |
| T5Trigger | 2 | 286 |
| minLgEnergySD | 17.5 | 286 |
| badPeriodsRejectionFromFile | - | 284 |

Table B.2: Number of HD reconstructed Pierre Auger Observatory events that passed individual SD cuts following their selection through the $X_{\max}$ cuts; nTot corresponds to the total number of showers processed.

| Cut | Parameter | Events passed |
|---|---|---|
| nTot | - | 267716 |
| !isCLF | - | 267716 |
| !isXLF | - | 267716 |
| keepHECOorCoihuecoHEAT | 18.1 | 266892 |
| eyeCut | 1111 | 255217 |
| badFDPeriodRejection | - | 245250 |
| minMeanPixelRMSMergedEyes | (17, 6, 110000) | 245250 |
| minMeanPixelRMSSimpleEye | (17, 11111) | 230776 |
| !badPixels | 1 | 221464 |
| good10MHzCorrection | - | 220060 |
| hasMieDatabase | - | 197133 |
| maxVAOD | 0.1 | 182283 |
| cloudCutXmaxPRD14 | 1 | 132228 |
| maxZenithFD | 90 | 132228 |
| minLgEnergyFD | 1e-20 | 126002 |
| skipSaturated | - | 125391 |
| minPBrass | 0.9 | 119502 |
| maxPBrassProtonIronDiff | 0.05 | 118130 |
| minLgEnergyFD | 19.2 | 1868 |
| FidFOVICRC13 | (40, 20) | 771 |
| xMaxObsInExpectedFOV | (40, 20) | 747 |
| maxDepthHole | 20 | 741 |
| profileChi2Sigma | (3, -1.1) | 698 |
| depthTrackLength | 200 | 698 |

Table B.3: Number of Pierre Auger Observatory events reconstructed using the SD geometry that passed individual $X_{\max}$ cuts; nTot corresponds to the total number of eye-reconstructed events processed.

| Cut | Parameter | Events passed |
|---|---|---|
| nTot | - | 506 |
| !lightning | - | 506 |
| minRecLevel | 3 | 506 |
| maxZenithSD | 60 | 398 |
| T4Trigger | 2 | 398 |
| T5Trigger | 2 | 292 |
| minLgEnergySD | 17.5 | 292 |
| badPeriodsRejectionFromFile | - | 290 |

Table B.4: Number of Pierre Auger Observatory events reconstructed using the SD geometry that passed individual SD cuts following their selection through the $X_{\max}$ cuts; nTot corresponds to the total number of showers processed.

| Cut | Parameter | Events passed |
|---|---|---|
| nTot | - | $1.47 \cdot 10^6$ |
| !isCLF | - | $1.47 \cdot 10^6$ |
| !isXLF | - | 1473154 |
| keepHECOorCoihuecoHEAT | 18.1 | 1467715 |
| eyeCut | 1111 | 1394222 |
| badFDPeriodRejection | - | 1329582 |
| minMeanPixelRMSMergedEyes | (17, 6, 110000) | 1329582 |
| minMeanPixelRMSSimpleEye | (17, 11111) | 1233904 |
| !badPixels | 1 | 1153093 |
| good10MHzCorrection | - | 1137801 |
| hasMieDatabase | - | 1020789 |
| maxVAOD | 0.1 | 945659 |
| cloudCutXmaxPRD14 | 1 | 681752 |
| maxZenithFD | 90 | 678754 |
| minLgEnergyFD | 1e-20 | 678153 |
| skipSaturated | - | 677814 |
| minLgEnergyFD | 19.2 | 7684 |
| FidFOVICRC13 | (40, 20) | 864 |
| xMaxObsInExpectedFOV | (40, 20) | 766 |
| maxDepthHole | 20 | 757 |
| profileChi2Sigma | (3, -1.1) | 695 |
| depthTrackLength | 200 | 693 |
| maxZenithFD | 60 | 547 |

Table B.5: Number of stereo reconstructed Pierre Auger Observatory events that passed individual $X_{\max}$ cuts; nTot corresponds to the total number of eye-reconstructed events processed.

| Cut | Parameter | Events passed |
|---|---|---|
| nTot | - | 2952 |
| minRecLevel | 3 | 2952 |
| maxZenithSD | 60 | 2643 |
| T4Trigger | 2 | 2643 |
| T5Trigger | 2 | 2636 |
| minLgEnergySD | 17.5 | 2636 |

Table B.7: Number of HD reconstructed CORSIKA simulated showers that passed individual SD cuts following their their selection through the $X_{\max}$ cuts; nTot corresponds to the total number of showers processed.

| Cut | Parameter | Events passed |
|---|---|---|
| nTot | - | 18282 |
| keepHECOorCoihuecoHEAT | 18.1 | 14639 |
| eyeCut | 1111 | 14461 |
| maxZenithFD | 90 | 14049 |
| minLgEnergyFD | 1e-20 | 13875 |
| skipSaturated | - | 13435 |
| minLgEnergyFD | 19.2 | 13417 |
| FidFOVICRC13 | (40, 20) | 5930 |
| xMaxObsInExpectedFOV | (40, 20) | 5672 |
| maxDepthHole | 20 | 5608 |
| profileChi2Sigma | (3, -1.1) | 5289 |
| depthTrackLength | 200 | 5288 |
| hybridTankTrigger | 2 | 5260 |
| maxCoreTankDist | 1500 | 5250 |

Table B.6: Number of HD reconstructed CORSIKA simulated showers that passed individual $X_{\max}$ cuts; nTot corresponds to the total number of eye-reconstructed events processed.

| Cut | Parameter | Events passed |
|---|---|---|
| nTot | - | 14780 |
| keepHECOorCoihuecoHEAT | 18.1 | 14616 |
| eyeCut | 1111 | 14453 |
| maxZenithFD | 90 | 14453 |
| minLgEnergyFD | 1e-20 | 14190 |
| skipSaturated | - | 13750 |
| minLgEnergyFD | 19.2 | 13740 |
| FidFOVICRC13 | (40, 20) | 6328 |
| xMaxObsInExpectedFOV | (40, 20) | 6040 |
| maxDepthHole | 20 | 5991 |
| profileChi2Sigma | (3, -1.1) | 5716 |
| depthTrackLength | 200 | 5716 |

Table B.8: Number of CORSIKA simulated showers reconstructed using the SD geometry that passed individual $X_{\max}$ cuts; nTot corresponds to the total number of eye-reconstructed events processed.

| Cut | Parameter | Events passed |
|---|---|---|
| nTot | - | 3041 |
| minRecLevel | 3 | 3041 |
| maxZenithSD | 60 | 2647 |
| T4Trigger | 2 | 2647 |
| T5Trigger | 2 | 2643 |
| minLgEnergySD | 17.5 | 2643 |

Table B.9: Number of CORSIKA simulated showers reconstructed using the SD geometry that passed individual SD cuts following their their selection through the $X_{\max}$ cuts; nTot corresponds to the total number of showers processed.

| Cut | Parameter | Events passed |
|---|---|---|
| nTot | - | 12707 |
| keepHECOorCoihuecoHEAT | 18.1 | 12459 |
| eyeCut | 1111 | 12459 |
| maxZenithFD | 90 | 11125 |
| minLgEnergyFD | 1e-20 | 10979 |
| skipSaturated | - | 10633 |
| minLgEnergyFD | 19.2 | 10583 |
| FidFOVICRC13 | (40, 20) | 4749 |
| xMaxObsInExpectedFOV | (40, 20) | 4607 |
| maxDepthHole | 20 | 4575 |
| profileChi2Sigma | (3, -1.1) | 4291 |
| depthTrackLength | 200 | 4291 |
| maxZenithFD | 60 | 3810 |

Table B.10: Number of stereo reconstructed CORSIKA simulated showers that passed individual $X_{\max}$ cuts; nTot corresponds to the total number of eye-reconstructed events processed.